



HAL
open science

New performing hydroxyapatite-based catalysts in dry-reforming of methane

Thanh Son Phan, Doan Pham Minh

► **To cite this version:**

Thanh Son Phan, Doan Pham Minh. New performing hydroxyapatite-based catalysts in dry-reforming of methane. *International Journal of Hydrogen Energy*, 2023, 48 (79), pp.30770-30790. 10.1016/j.ijhydene.2023.04.273 . hal-04094935

HAL Id: hal-04094935

<https://imt-mines-albi.hal.science/hal-04094935v1>

Submitted on 11 May 2023

HAL is a multi-disciplinary open access archive for the deposit and dissemination of scientific research documents, whether they are published or not. The documents may come from teaching and research institutions in France or abroad, or from public or private research centers.

L'archive ouverte pluridisciplinaire **HAL**, est destinée au dépôt et à la diffusion de documents scientifiques de niveau recherche, publiés ou non, émanant des établissements d'enseignement et de recherche français ou étrangers, des laboratoires publics ou privés.

New performing hydroxyapatite-based catalysts in dry-reforming of methane

Thanh Son Phan ^{a,b}, Doan Pham Minh ^{a,*}

^a Université de Toulouse, IMT Mines Albi, CNRS UMR 5302, Centre RAPSODEE, Campus Jarlard, F-81013, Albi Cedex 09, France

^b Faculty of Chemical Engineering, University of Science and Technology, The University of Da Nang, Da Nang City, 550000, Viet Nam

Keywords:

Dry reforming of methane

Syngas

Hydrogen

Hydroxyapatite

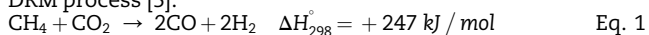
Catalyst

Nickel

Dry reforming of methane (DRM) is a promising process for the production of synthetic gas from carbon dioxide and methane. However, the design of a performing catalyst for this reaction is still challenging since catalyst deactivation usually takes place, principally by thermal sintering at high temperatures (700–950 °C) and by carbon deposition. In this work, calcium hydroxyapatite (HAP) and HAP-doped magnesium (Mg_HAP) supported nickel catalysts were synthesized by wet precipitation method, characterized by various physico-chemical and thermal techniques, and evaluated in DRM reaction. Outstanding catalytic performance in DRM could be obtained with Ni/ HAP and Ni/Mg_HAP catalysts, thanks to a tunable acidity-basicity of these supports, a strong metal-support interaction, and a good thermal stability of nickel nanoparticles. H₂ and CO were the main products, with stable selectivity up to 85 ± 3%, while H₂O and solid carbon were byproducts with 5–10% of selectivity.

Introduction

Dry reforming of methane (DRM) is an attractive catalytic process for synthetic gas (syngas, a gas mixture rich in CO and H₂) production from methane and carbon dioxide, which are the two main greenhouse gases (Eq. (1)). Syngas is well known for its versatility, which can be used to feed different chemical processes such as water-gas shift, alcohol synthesis, catalytic methanation, Fischer–Tropsch synthesis, etc. [1]. Despite the importance of DRM reaction, its industrial deployment still meets difficulties. In fact, the standard enthalpy of the DRM reaction is very high (Eq. (1)), so this reaction is highly endothermic. Thus, high reaction temperatures, typically in the range of 700–950 °C, are needed to thermodynamically favor high reaction conversions [2–4]. Even at high temperature, DRM reaction requires the utilization of a catalyst to reach high kinetics. Under high reaction temperatures, thermal sintering of the catalyst can take place, in particular in the case of metal nanoparticles supported on a support [5]. Moreover, the reaction of CH₄ with CO₂ can also be impacted by various side reactions, such as reverse water-gas shift, methane cracking, Boudouard reaction etc. [2, 3], leading to the formation of byproducts. Among them, solid carbon has been reported in most of publications on DRM reaction [3], which also causes catalyst deactivation in DRM. Developing a highly-performing catalyst, which resists to solid carbon formation and to thermal sintering is among the main objectives for DRM process [5].



To-date, nickel-based catalysts, under the form of nickel nanoparticles supported on a solid support have largely been reported for DRM reaction [6,7]. To a lesser extend, other transition metal-based catalysts (e.g. iron, cobalt, copper) [8–10], noble metal-based catalysts (e.g. Pt, Pd, Ru etc.) [11,12], or nickel-containing bimetallic catalysts (e.g. Ni-Co, Ni-Fe, Ni-Co, etc.) have also been reported [13–16]. About catalyst supports, the conventional materials such as alumina, silica, ceria, zirconia, zeolites, mixed oxides, etc. have usually been reported [17–19]. As recently reviewed by Hambali et al. [20], the common criteria required for a robust DRM catalyst are as follows: a good metal dispersion, a strong metal-support interaction, a high specific surface area, a mobility of surface oxygen, and an adequate acidity/basicity. Thus, catalyst support plays crucial role in DRM reaction. The exploration of new promising catalyst supports, such as hydroxyapatite (HAP, Ca₁₀(PO₄)₆(OH)₂) is recommended in order to design new performing DRM catalysts. In fact, HAP has several advantages for a catalyst supports such as a possible high porous volume and high specific surface area, high thermal stability, exceptional ion exchange capacity, and tunable acid-base property [21]. HAP-supported metal (Ni, Pt, Ru or Ni-Co) catalysts have been investigated in DRM reaction [22–30], showing high catalytic performance in comparison with catalysts prepared from conventional supports (Table 1) [24]. One of the main advantages of HAP supports is related to the controllability of the acidity/basicity, which can be achieved by varying the molar ratio of Ca/P, and/or by partially substituting Ca²⁺ cations by other divalent cations such as Mg²⁺. While the impact of the Ca/P ratio has been investigated by Boukha et al. [23], the

impact of Mg addition to HAP support is not studied yet in DRM reaction, to the best of our knowledge. Thus, the objective of the present study is to investigate the impact of the Ca/P ratio and the partial substitution of Ca²⁺ by Mg²⁺ in HAP structure on the catalytic performance of Ni supported catalysts.

Experimental

Preparation of apatitic supports

Calcium hydroxyapatite (HAP) supports

HAP supports were prepared by wet precipitation method, according to the method described elsewhere [31]. Briefly, calcium nitrate (Ca(NO₃)₂·4H₂O 99% purity, CAS: 13477-34-4) and ammonium dihydrogen phosphate (NH₄H₂PO₄, 98% purity, CAS: 7722-76-1), which were purchased from Fisher Scientific, were used as starting materials. Aqueous solutions of calcium nitrate (0.89 M) and ammonium dihydrogen phosphate (0.34 M) were prepared using permuted water at room temperature, and their pH values were fixed at 10.7 et 10.3, respectively, using an aqueous solution of NH₄OH (35 wt%, CAS: 1336-21-6, from Fisher Scientific). The synthesis was performed in a glass reactor, thermostated at 40 °C and stirred at 400 rpm, by adding the solution of NH₄H₂PO₄ into the solution of Ca(NO₃)₂. The volume of each solution was calculated to obtain theoretical molar ratio of Ca to P (Ca/P) of 1.55, 1.67 and 1.75, which correspond to calcium-deficient, stoichiometric, and calcium-surplus HAP, respectively. The mixture was kept under a constant pH of 9.6 (by using the solution of NH₄OH mentioned above) for 48 h. A white precipitate was formed, which was filtered and washed several times and dried at 105 °C overnight in an electrical oven. Finally, HAP supports were crushed and sieved to obtain grains in the range of 125–315 μm (see Supplementary information SI 1), which were later used for preparing Ni/HAP catalysts. Three HAP supports were synthesized which are named as follows: HAP1.55, HAP1.67 and HAP1.75, resulting from three theoretical values of the Ca/P ratio mentioned above.

Calcium hydroxyapatite-doped magnesium (Mg_HAP) supports

Mg_HAP supports were prepared by the same procedure described above for HAP supports, by replacing Ca(NO₃)₂

Table 1 – Reactivity of Ni-based catalysts in DRM reaction at 700 °C and ambient pressure; nd: not determined. Ni/Ca-HA2: a HAP-supported nickel catalyst. Adapted with permission of Elsevier [24].

Catalyst	Metal content (wt.%)	Catalyst weight (mg)	CH ₄ /CO ₂ conversion (%)	Time on stream (h)
NiLa ₂ O ₃ /ZrO ₂	Ni: 5	200	70/nd	50
Ni/Al ₂ O ₃	Ni: 6.6	180	67/75	24
Ni-Mg/Al ₂ O ₃	Ni: 5, Mg: 3	200	77/nd	22
Ni/CeO ₂	Ni: 5	50	40-15/ 80-40	12
Ni/Ca-HA2	Ni: 5	300	78-66/ 84-73	90

aqueous solution by a mixture solution containing both $\text{Ca}(\text{NO}_3)_2$ and $\text{Mg}(\text{NO}_3)_2$. The latter ($\text{Mg}(\text{NO}_3)_2$, >98% purity, CAS: 13446-18-9) was also purchased from Fischer Scientific. The concentration of each solution was calculated to obtain three Mg_HAP supports with the theoretical values of molar ratio of $(\text{Ca} + \text{Mg})/\text{P} = 1.67$, and $\text{Mg}/\text{Ca} = 0.1, 0.3$ and 0.5 , which led to three material named respectively 0.1 Mg_HAP, 0.3 Mg_HAP and 0.5 Mg_HAP. The dried Mg_HAP supports were also crushed and sieved to obtain grains of 125–315 μm , which were later used for preparing Ni/Mg_HAP catalysts.

Preparation of nickel supported catalysts

Grains of HAP and Mg-HAP supports were first calcined at 500 °C in the air to avoid all further structural evolution of the apatitic materials. The deposition of nickel on the surface of the supports was carried out by the conventional incipient wetness impregnation method [24, 25], using nickel nitrate precursor ($\text{Ni}(\text{NO}_3)_2 \cdot 6\text{H}_2\text{O}$, 98% purity, CAS: 13478-00-7, from Fisher Scientific). The theoretical value of nickel loading was fixed at 5 wt%. After impregnation, the mixture was dried at 105 °C overnight, calcined at 700 °C under the air for 3 h to convert nickel precursor into nanoparticles of nickel oxides. Thus, from six HAP and Mg_HAP supports, six nickel supported catalysts were obtained, which are named as follows: 5Ni/HAP1.55, 5Ni/HAP1.67, 5Ni/HAP1.75, 5Ni/0.1 Mg_HAP, 5Ni/0.3 Mg_HAP, and 5Ni/0.5 Mg_HAP (Table 2).

Characterization methods

Elemental analysis was carried out with an ICP-AES (Inductively Coupled Plasma-Atomic Emission Spectroscopy) HORIBA Jobin Yvon Ultima 2 apparatus. Before analysis, calcined catalysts were dissolved in *aqua regia* (a mixture of concentrated HCl and HNO_3 acids).

Fourier transformed infrared (FTIR) spectra of the calcined catalysts were recorded within 4000 à 500 cm^{-1} wavelength range, with a SHIMADZU 8400S spectrometer.

Thermogravimetry coupled with differential thermal analysis (TG-DTA) were performed with a SDT Q600 (TA Instru-ment), while TG coupled with mass spectroscopy (TG-MS) analysis was done with a STA 409 PC (Netzsch) and a GSD 320 (Pfeiffer Vacuum OmniStar). For each analysis, samples of calcined catalysts (around 30 mg) were heated from 30 to 1000 °C under the air (100 NmL/min), with a heating rate of 10 °C/min.

X-rays diffraction (XRD) patterns were recorded in the range of 2θ of 10–80 degrees, using a X'pert Pro MPD

(PANalytical) diffractometer. The identification of crystalline phases was carried out with the International Centre for Diffraction Data (ICDD) and Crystallography Open Database (COD) databases. These analyses were conducted with catalysts calcined at 500 and 700 °C under the air. From XRD results, the crystallite size of nickel oxide is calculated according to the Scherrer equation (Eq. 2) [32]. The calculation was done with three main diffraction peaks of NiO crystallites at 2θ of 37.33, 43.94, and 62.97 degrees, which allowed obtaining the average NiO crystallite size.

$$d = \frac{k \cdot \lambda}{\text{FWHM} \cdot \cos \theta} \quad \text{Eq. 2}$$

where d is the crystallite size of nickel oxide (nm), k is a dimensionless shape factor which has usually the value of 0.9, λ is the X-ray wavelength (nm), θ is the Bragg diffraction angle (°), FWHM is the full-width at half-maximum of the considered peak (Rad).

Scanning electron microscopy (SEM) analysis was carried out with a Philips XL30 ESEM FEG apparatus. SEM images were recorded using both Secondary Electron (SE) and Back-scattered Electron (BSE) detectors. Transmission electron microscopy coupled with energy-dispersive X-ray spectroscopy (TEM-EDX) were also conducted, by using both FEG JEOL JEM 2100F and JEOL1400 machines.

Specific surface area and pore size distribution of the calcined catalysts were obtained from nitrogen adsorption-desorption isotherms. These isotherms were recorded with a Micromeritics Tristar II 3020 apparatus at 77 K. Before analysis, solid samples were degassed at 105 °C and 50–100 mbar for 24 h, using a Micromeritics 3FLEX machine. From the isotherms, the specific surface area was calculated by the Brunauer – Emmett – Teller (BET) model, while the pore size distribution was obtained by the BJH (Barrett-Joyner-Halenda) model, since the prepared catalysts are mesoporous materials.

Temperature-programed reduction (TPR) was carried out with dried catalysts, using a Micromeritics Autochem 2920 machine. For each analysis, around 100 mg of dried catalyst were placed in a U-shape quartz reactor, heated by an electric oven. The reactor was heated from 30 to 700 °C (10 °C/min) under a flux of 4%vol. H_2/He (100 NmL/min). The reduction was detected by a Thermal Conductivity Detector (TCD). By using this same Micromeritics Autochem 2920 machine, temperature-programed desorption (TPD) was also performed, using both CO_2 (CO_2 -TPD) and NH_3 (NH_3 -TPD) as probe molecules, in order to analyze respectively basic and acidic sites of the catalysts. For a given analysis, 100 mg of dried catalyst were first reduced under H_2 at 700 °C for 2 h. Then, it

Table 2 – Results of elemental analysis by ICP-AES of the prepared catalysts; in brackets: theoretical values.

Catalyst	Molar ratio			Weight percentage (%)	
	Ca/P (theoretical value)	Mg/Ca (theoretical value)	(Ca + Mg)/P (theoretical value)	% Mg (theoretical value)	% Ni (theoretical value)
5Ni/HAP1.55	1.61 (1.55)	–	–	–	3.75 ± 0.10 (5)
5Ni/HAP1.67	1.73 (1.67)	–	–	–	3.96 ± 0.20 (5)
5Ni/HAP1.75	1.74 (1.75)	–	–	–	3.91 ± 0.28 (5)
5Ni/0.1 Mg_HAP	1.60 (1.52)	0.14 (0.10)	1.82 (1.67)	2.4 (2.2)	3.96 ± 0.10 (5)
5Ni/0.3 Mg_HAP	1.25 (1.28)	0.44 (0.30)	1.81 (1.67)	6.9 (5.8)	4.07 ± 0.33 (5)
5Ni/0.5 Mg_HAP	1.10 (1.11)	0.53 (0.50)	1.64 (1.67)	6.2 (8.5)	3.98 ± 0.27 (5)

was cooled down to 100 °C under He. Then, the adsorption of CO₂ or NH₃ was done at 100 °C under a flux (50 NmL/min) of 5% CO₂/N₂ or 5%NH₃/N₂, respectively, for 60 min. After a purge with a He flux at 100 °C, the CO₂-TPD or NH₃-TPD was recorded by heating the sample to 800 °C (10 °C/min heating rate) under He. The desorption was detected by a TCD detector.

Catalytic reactor and procedure of DRM reaction

The scheme and a photo of the fixed-bed reactor used in this work is presented in Supplementary information SI 2. The tubular reactor is made by alumina refractory ceramic, with an inner diameter of 8 mm and a length of 25 cm. For each reaction, the reactor was filled with inert alumina powder (<3 m²/g), followed by a mixture of calcined catalyst (340 mg) diluted with inert alumina powder (340 mg), and completed with inert alumina powder. The quantity of each layer of inert alumina powder was calculated to fix the catalyst bed at the center of the reactor, which can be homogeneously heated by the oven. The pressure drop observed in the reactor varied between 0.5 and 0.9 bar, depending on the gas flowrate used. The total pressure inside the reactor was controlled by a manual device, which can work between 1 and 50 bar. The temperature of the catalyst bed was controlled by a thermocouple set at the center of the bed. The reactor was fed with different gas bottles under high pressure. The flowrate of each gas was controlled by a mass-flow controller (MFC), which allowed obtaining the desired feeding composition. To start a DRM reaction, the reactor was heated under N₂ flux (70 NmL/min) up to 700 °C. Then, an in-situ reduction took place under 10%vol.H₂/N₂ flux (70 NmL/min) for 2 h. Then, the temperature of the reactor was set to the desired temperature (if needed), and the DRM re-action started by feeding the reactor with a mixture of CH₄, CO₂, and N₂.

At the outlet of the reactor, a water trap containing silica gel was used to quantify water formed as a byproduct of the DRM reaction. The dried gas mixture at the outlet of this trap was analyzed by a μ-GC (MyGC model, from Agilent). The total flowrate of this dried gas was measured by a Pro Flow 6000 flowmeter (from Restek). This total gas flowrate and its composition obtained by μ-GC allowed calculating the flowrate (moles/min) of each gas in the mixture. The conversion (X, %) and the selectivity (S, %) of the DRM reaction were calculated by the following equations.

$$X_{CH_4}(\%) = \frac{Q_{CH_4}^{inlet} - Q_{CH_4}^{outlet}}{Q_{CH_4}^{inlet}} \times 100 \quad \text{Eq. 3}$$

$$X_{CO_2}(\%) = \frac{Q_{CO_2}^{inlet} - Q_{CO_2}^{outlet}}{Q_{CO_2}^{inlet}} \times 100 \quad \text{Eq. 4}$$

$$S_{H_2}(\%) = \frac{Q_{H_2}^{formed}}{2 \times (Q_{CH_4}^{inlet} - Q_{CH_4}^{outlet})} \times 100 \quad \text{Eq. 5}$$

$$S_{CO}(\%) = \frac{Q_{CO}^{formed}}{2 \times (Q_{CO_2}^{inlet} - Q_{CO_2}^{outlet})} \times 100 \quad \text{Eq. 6}$$

$$S_C(\%) = \frac{Q_C^{formed}}{(Q_{CH_4}^{inlet} - Q_{CH_4}^{outlet}) + (Q_{CO_2}^{inlet} - Q_{CO_2}^{outlet})} \times 100 \quad \text{Eq. 7}$$

$$S_{H_2O}(\%) = \frac{Q_{H_2O}^{formed}}{2 \times (Q_{CO_2}^{inlet} - Q_{CO_2}^{outlet})} \times 100 \quad \text{Eq. 8}$$

where: X_{CH₄} and X_{CO₂} are CH₄ and CO₂ conversions, respectively; S_{H₂}, S_{CO}, S_C and S_{H₂O} are selectivity in hydrogen, carbon monoxide, solid carbon, and water, respectively; Q_{CH₄}^{inlet} and Q_{CH₄}^{outlet} are molar methane flowrate (moles/min) at the reactor inlet and reactor outlet, respectively; Q_{CO₂}^{inlet} and Q_{CO₂}^{outlet} are molar carbon dioxide flowrate (moles/min) at the reactor inlet and reactor outlet, respectively; Q_{CO}^{formed}, Q_{H₂}^{formed}, and Q_{H₂O}^{formed} are molar flowrate (moles/min) of CO, H₂ and H₂O, respectively, which are formed during the reaction; and Q_C^{formed} is the flowrate of solid carbon calculated from the carbon balance. In reality, it is not possible to measure Q_C^{formed} during the DRM reaction for this experimental setup.

Results and discussion

Catalyst characterization

Elemental analysis

The results of ICP-AES analysis for the fresh catalysts are presented in Table 2. Among three catalysts prepared from HAP supports (without Mg addition), 5Ni/HAP1.55 was a calcium-deficient material with the analytical Ca/P ratio equal to 1.61, while the two others were calcium-surplus materials with the similar analytical Ca/P ratio equal to 1.73 and 1.74. On the other hand, stoichiometric HAP could not be obtained. This could be explained by the fact that, HAP synthesis is a delicate process which depends on a set of parameters such as the nature and the addition order of calcium and phosphorus precursor, the aging time, the pH control, and the washing procedure [33–35]. For three catalysts prepared from Mg_HAP supports, the analytical values of the Ca/P ratio were close to the corresponding theoretical values. However, the analytical values of the Mg/Ca ratio are notably higher than the corresponding theoretical values. This suggests a part of Ca²⁺ cations were not precipitated. Despite this calcium loss, the (Ca + Mg)/P ratio obtained by ICP-AES were higher than the corresponding theoretical values for the two catalysts 5Ni/0.1 Mg_HAP and 5Ni/0.3 Mg_HAP, meaning a loss of phosphate also took place under the form of soluble ions in the filtrate. On the other hand, for 5Ni/0.5 Mg_HAP, the (Ca + Mg)/P ratio was slightly smaller than the theoretical one, which is explained by a loss of Ca²⁺ and/or Mg²⁺ cations during the synthesis. These results highlighted the delicacy of the synthesis of apatitic materials, as recently reported by El Jemli et al. [33].

Nickel loading of the prepared catalysts varied in the range of 3.75 ± 0.10 and 4.07 ± 0.33 wt%, which is smaller than the theoretical value of 5 wt%. Possible, a loss of nickel (e.g. nickel fixed on the wall of the flash) took place during the catalyst

synthesis. This loss can be significant for the preparation of small quantity of catalyst (*e.g.* some grams), as in this study. This phenomenon was usually observed in the heterogeneous catalysis [33,36].

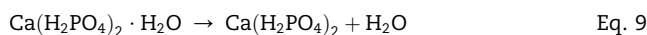
FTIR

Fig. 1 shows the FTIR spectra of the HAP and Mg_HAP supports. Characteristic peaks of the apatitic structure were observed. The peaks at 565, 603, 960, 1037, and 1091 cm^{-1} could be attributed to the vibration of $(\text{PO}_4)^{3-}$ groups, while the peaks at 636 and 3572 cm^{-1} belong to the vibration of OH^- groups [37,38]. The peaks at 873, 1414 and 1454 cm^{-1} could be due to the presence of CO_3^{2-} groups. The latter could be inserted to the apatitic structure during the synthesis, by the dissolution of CO_2 from the air in the solution mixture, and by the fixation of CO_2 from the air in contact with the solid supports [39]. In addition, the peaks of CO_3^{2-} groups indicate the formation of B-type carbonated apatite (substitution of phosphate groups by carbonate groups) [40,41]. This observation agrees with the ICP-AES results, since the analytical values of Ca/P and (Ca + Mg)/P ratios were higher than the corresponding theoretical ones. Finally, the presence of Mg in Mg_HAP supports seemed to have an impact on the apatitic structure, causing an enlargement as well as an intensity diminution of the PO_4^{3-} bands in the elongation region (1030 cm^{-1}) and the bend region (565 cm^{-1}) [42]. Similar FTIR spectra were also obtained with the calcined nickel catalysts prepared from these six supports (results not shown). Nickel oxide nanoparticles, as evidenced later by SEM and TEM analyses, did not lead to a notable change of FTIR signals of the supports.

TG-DTA and TG-MS

Fig. 2 presents the evolution of the mass, and CO_2 and H_2O emission during TG and TG-MS analyses of the supports. Note that DTG curves were the derivative of the corresponding TG curves, which better highlight the mass evolution than TG curves. DTA results are not shown since only endothermal phenomena were observed. Thus, within 30 and 200 $^\circ\text{C}$, several mass losses took place which were due to the departure of physisorbed water (below 100 $^\circ\text{C}$) and the possible dehydration of MCPM (mono-calcium phosphate monohydrate, $\text{Ca}(\text{H}_2\text{PO}_4)_2 \cdot \text{H}_2\text{O}$) between 100 and 200 $^\circ\text{C}$ according to

Eq. (9) [43]. In the range of 200–700 $^\circ\text{C}$, all the supports had small and consecutive mass losses, which could not be observed as net DTG peak. This was due to the dehydration and decarbonation as highlighted by TG-MS analysis (Fig. 2 (c) and (d)), which corresponds to the thermal behavior of apatitic materials [33]. In fact, in this temperature range, the dehydration could take place with superficial hydrogenophosphate groups such as H_2PO_4^- and HPO_4^{2-} [44], while the decarbonation could be due to the carbonate groups chemisorbed on the basic sites of these supports. In the temperature range of 700–1000 $^\circ\text{C}$, DTG peaks were observed for some materials, which could be also explained by dehydration and decarbonation. The dehydration in this zone (700–1000 $^\circ\text{C}$) could be either provoked by the condensation of HPO_4^{2-} groups, incorporated in the apatitic structure, into pyrophosphate (Eq.(10)), followed by the conversion of pyrophosphate into phosphate (Eq. (11)) [106], or the partial decomposition the apatitic components into β -TCP [45]. The temperature of these dehydration decreased when the Mg loading in Mg_HAP supports increased, as a consequence of Mg incorporation in the apatitic structure [46,47]. The decarbonation in this zone (700–1000 $^\circ\text{C}$) was due to the departure of carbonate anions, inserted in the apatitic structure [25]. For all six supports, the mass loss did not finish at 1000 $^\circ\text{C}$, which could be explained by the partial dehydration of hydroxyl groups of the apatitic structure at high temperature [48].



XRD

XRD diffractograms of all the catalysts calcined at 500 and 700 $^\circ\text{C}$ under the air are displayed in Fig. 3. For Ni/HAP1.55, Ni/HAP1.67, and Ni/HAP1.75 calcined at 500 $^\circ\text{C}$, characteristic peaks of the crystalline phase of the apatitic structure at 2θ angle of 25.9, 31.8, 32.9, 46.8 and 49.7 degrees were observed [33,49]. When these catalysts were calcined at 700 $^\circ\text{C}$, the same peaks were also observed, with a better crystallinity. In addition, a new peak at 2θ angle of 32.2 degrees appeared which also corresponded to the (112) crystalline plan of the apatitic

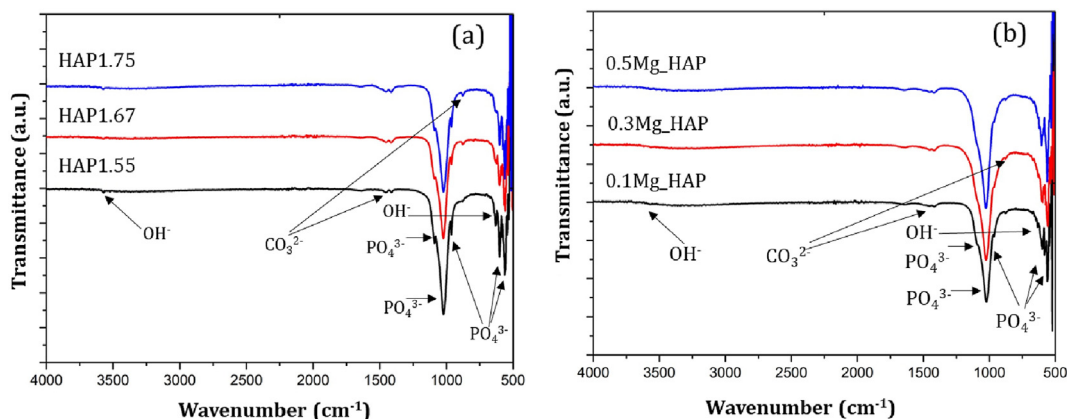


Fig. 1 – FTIR spectra of the HAP supports (a), and Mg_HAP supports (b).

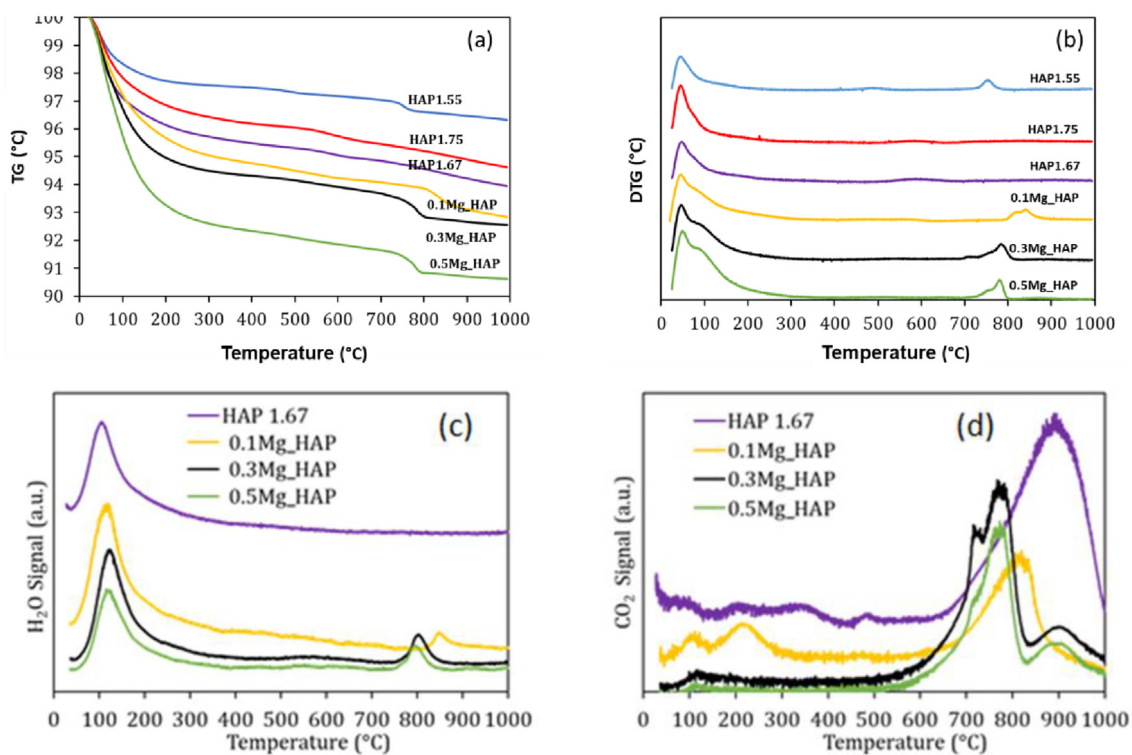


Fig. 2 – Thermal behavior of HAP and Mg_HAP supports: (a) and (b): TG and DTG signals during TG analysis, respectively; (c) and (d): H₂O and CO₂ emissions during TG-MS analysis, respectively.

structure. No diffraction peak of other compounds such as MCPM or TCP could be observed, which could be due to their low contents. For nickel, diffraction peaks at 2θ of 37.3, 43.4 and 63.5 degrees were observed, which could be attributed to nickel oxide (NiO).

For Mg_HAP supported nickel catalysts calcined at 500 °C, at low Mg content (2.2 wt% Mg in 5Ni/0.1 Mg_HAP), only peaks of the apatitic structure could be observed, which are similar to those of HAP supports. Other crystalline phases of Mg such as MgO or Mg(OH)₂ were not observed. Probably, at this low Mg content, Mg²⁺ cations were incorporated to the apatitic structure and partially replaced Ca²⁺ cations. When this catalyst was calcined at 700 °C, the same diffraction peaks were detected, accompanied with a new peak at 2θ of 32.2 degrees as already observed for Ni/HAP catalysts. For catalysts containing higher Mg contents (5Ni/0.3 Mg_HAP and 5Ni/0.5 Mg_HAP) calcined at 500 °C, the principal diffraction peaks of the apatitic structure at 2θ around 30–35 degrees are superimposed and formed a broad peak, which suggests a low crystallinity of these materials. In addition, mixed oxides of Mg and Ni could be also formed. When these catalysts were calcined at 700 °C, whitlockite (Ca₅₇Mg₆(PO₄)₄₂, ICDD: 96-901-2138) was formed as a new crystalline phase. The latter was already observed by Fadeev et al. [50] who employed the similar synthesis conditions (co-precipitation using the same Ca, Mg et P precursors). In addition, these authors evidenced the favorable effect of increasing Mg content on the formation of whitlockite. For all three nickel catalysts supported on Mg_HAP supports, the characteristic peaks of nickel oxide (NiO) at 2θ of 37.2, 43.2 and 63.52 degrees were observed. From

the XRD results, the average size of NiO crystallites could be calculated by the Scherrer equation, which varied in the range of 21.4 and 27.8 nm (Table 3).

SEM and TEM-EDX

All the six catalysts calcined at 700 °C were analyzed by SEM and TEM-EDX. As shows in Supplementary information SI 3, at low magnification, three HAP-supported nickel catalysts and 5Ni/0.1 Mg_HAP catalyst were composed of grains with relatively homogeneous and large size. On the other hand, 5Ni/0.3 Mg_HAP and 5Ni/0.5 Mg_HAP catalysts contained much smaller grains, since they were more brittle than the four other catalysts. High Mg content probably weakened the me-chanical strength of these materials.

At high SEM magnification, nickel oxide nanoparticles could be observed (Fig. 4). The size of nickel oxide nanoparticles seemed to be similar for all these catalysts. However, nickel oxide nanoparticles in 5Ni/0.3 Mg_HAP and 5Ni/0.5 Mg_HAP catalysts were less visible and had a lower frequency on their surface, in comparison with the other catalysts.

Fig. 5 shows TEM images and particle size distribution of four catalysts calcined at 700 °C. Two catalysts 5Ni/HAP1.75 and 5Ni/0.5 Mg_HAP were not analyzed by TEM since they are similar to 5Ni/HAP1.67 and 5Ni/0.3 Mg_HAP catalysts, as previously evidenced by different characterization techniques. Thus, all four catalysts showed nickel oxide nanoparticles in a large range of ca. 14–120 nm. These particles were generally not spherical. Some agglomerations could be also observed. From TEM images, the size distribution of nickel oxide

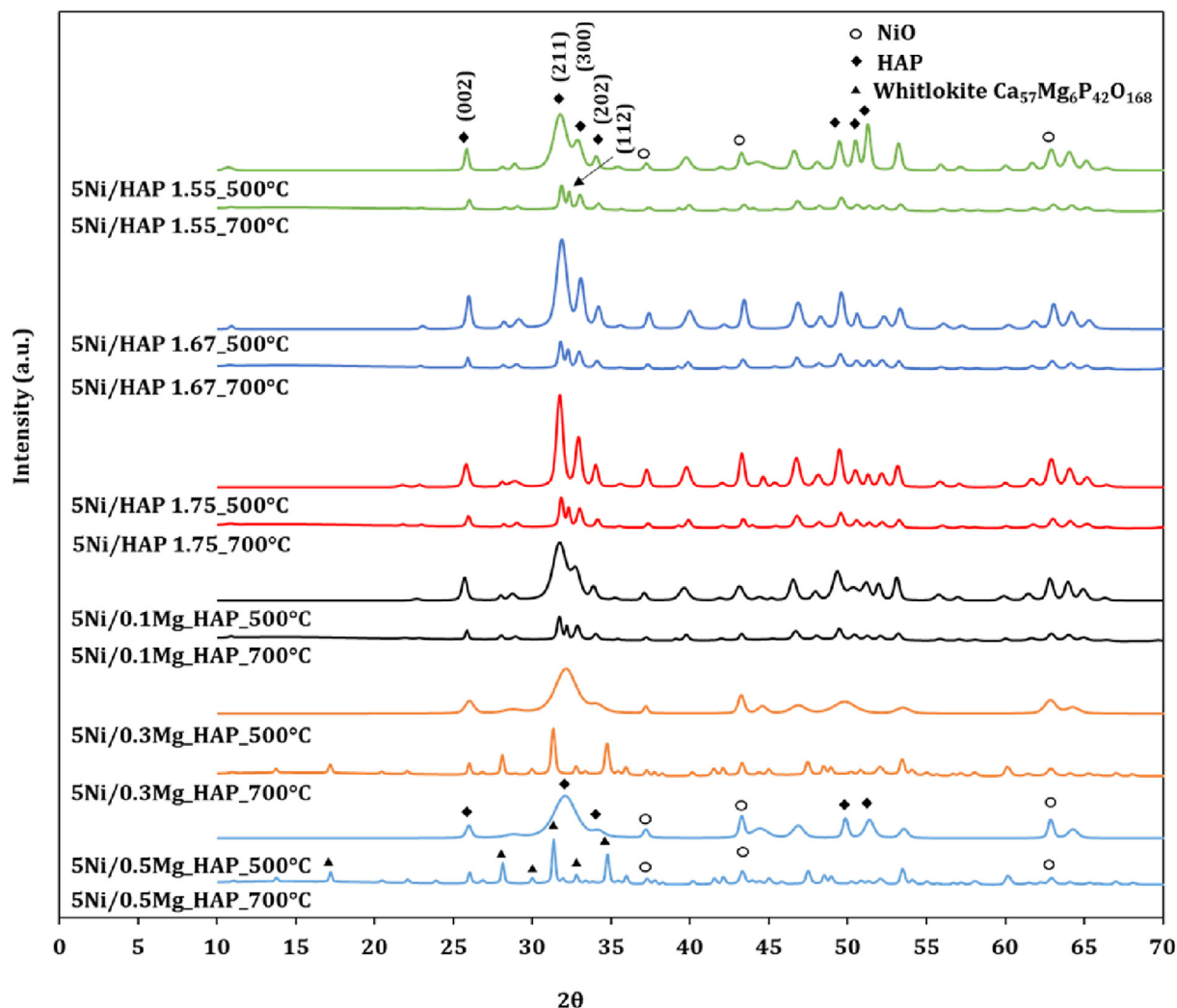


Fig. 3 – XRD diffractograms of HAP and Mg_HAP supported nickel catalysts, calcined at 500 (denoted as “catalyst_500 °C”) and 700 °C (denoted as “catalyst_700 °C”) under the air.

Table 3 – Comparison of average size of nickel oxide crystallites (by XRD) and nanoparticles (by TEM) of the prepared catalysts. n.a.: not available.

Catalyst	Average size of NiO crystallites by XRD (nm)	Average size of NiO nanoparticles by TEM (nm)
5Ni/HAP1.55	27.8 ± 6.7	39.5
5Ni/HAP1.67	24.4 ± 2.7	40.3
5Ni/HAP1.75	25.9 ± 2.9	n.a.
5Ni/0.1 Mg_HAP	22.0 ± 3.8	53.9
5Ni/0.3 Mg_HAP	26.6 ± 3.3	50.5
5Ni/0.5 Mg_HAP	21.4 ± 0.9	n.a.

nanoparticles could be obtained as shown in Fig. 5 (e). Most of nickel oxide nanoparticles were found in the large range of 14–70 nm. For two Ni/HAP catalysts, the particle size was impacted by the Ca/P ratio: the higher the Ca/P ratio was, the larger the particle size was. The average sizes of nickel oxide nanoparticles determined by TEM are summarized in Table 3, which are coherent with the average size of nickel oxide crystallites. Finally, EDX mapping was also performed with four catalysts analyzed by TEM above. For Ni/HAP catalysts, Ca and P were homogeneously distributed on the surface of catalyst grains, while Ni was mostly found under the form of

nanoparticles (see Supplementary information SI 4 and SI 5). For Ni/Mg_HAP catalysts, Ca, Mg and P were also homogeneously distributed on the surface of catalyst grains, as expected. This confirmed the combination of Mg with phosphate anions in the apatitic structure. About nickel, it was mostly found under the form of nanoparticles (see Supplementary information SI 6 and SI 7).

Nitrogen adsorption–desorption isotherms

Nitrogen adsorption-desorption isotherms of the supports and the catalysts are displayed in Fig. 6 (a) and (b). All of them

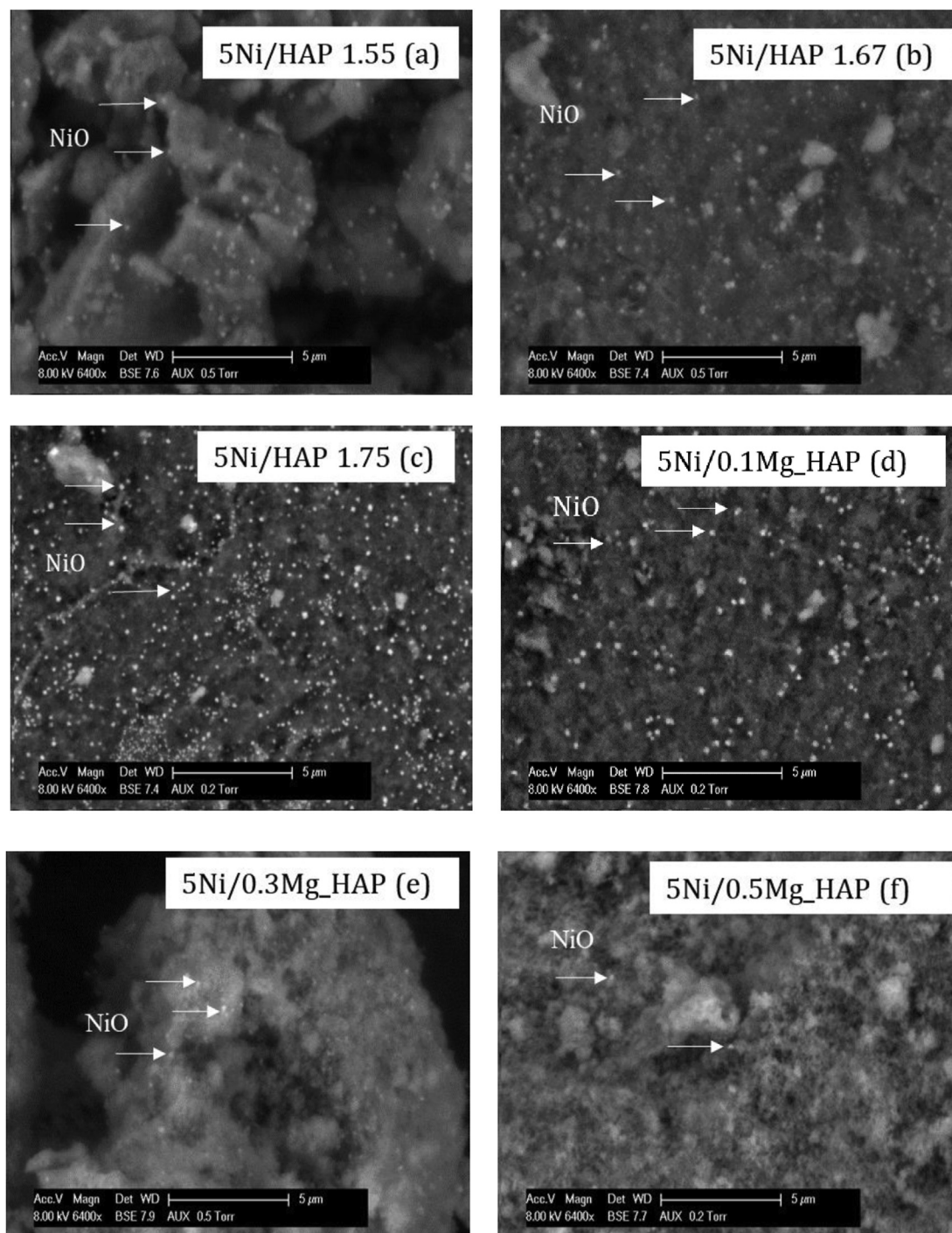


Fig. 4 – SEM images at high magnification of Ni/HAP and Ni/Mg_HAP catalysts.

belong to the type IV according to the IUPAC classification [51,52], indicating that these supports are mesoporous materials. The hysteresis loops of three HAP supports (Fig. 6 (a)) were of type H1, indicating the presence of pores of narrow size [51, 52]. This could be confirmed by the results of pore size distribution using the BJH method (Fig. 6 (c)). Each HAP support had a monomodal pore size distribution of ca. 22–31 nm (Table 4).

The support 0.1 Mg_HAP also had the H1 type hysteresis loop (Fig. 6 (b)) with a monomodal pore size distribution

(Fig. 6 (c)), which is similar to HAP supports. On the other hand, 0.3 Mg_HAP and 0.5 Mg_HAP supports presented H2 type hysteresis loops, which is characteristic for materials with slit-shaped pores of irregular sizes [51, 52]. The analysis of differential pore size distribution of these materials indicated the presence of pores in a large range, up to 120 nm (Fig. 6 (d)).

The deposition of nickel nanoparticles on the surface of HAP and Mg_HAP supports by incipient wetness impregnation method did not notably impact the shape of these

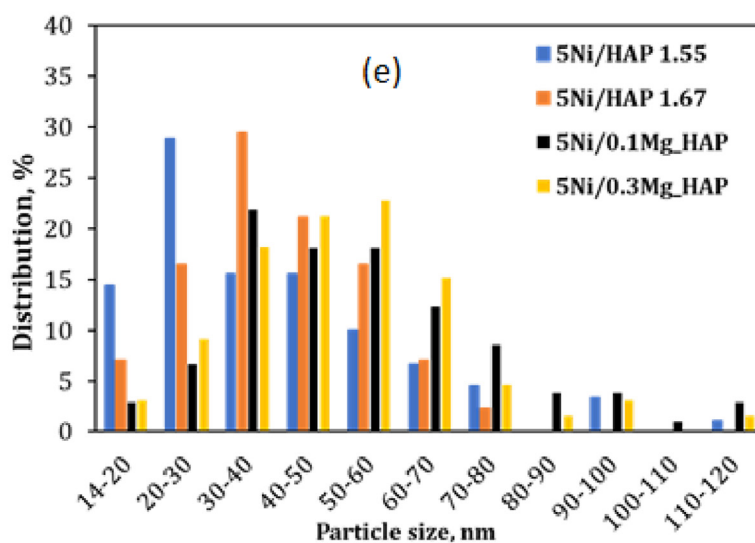
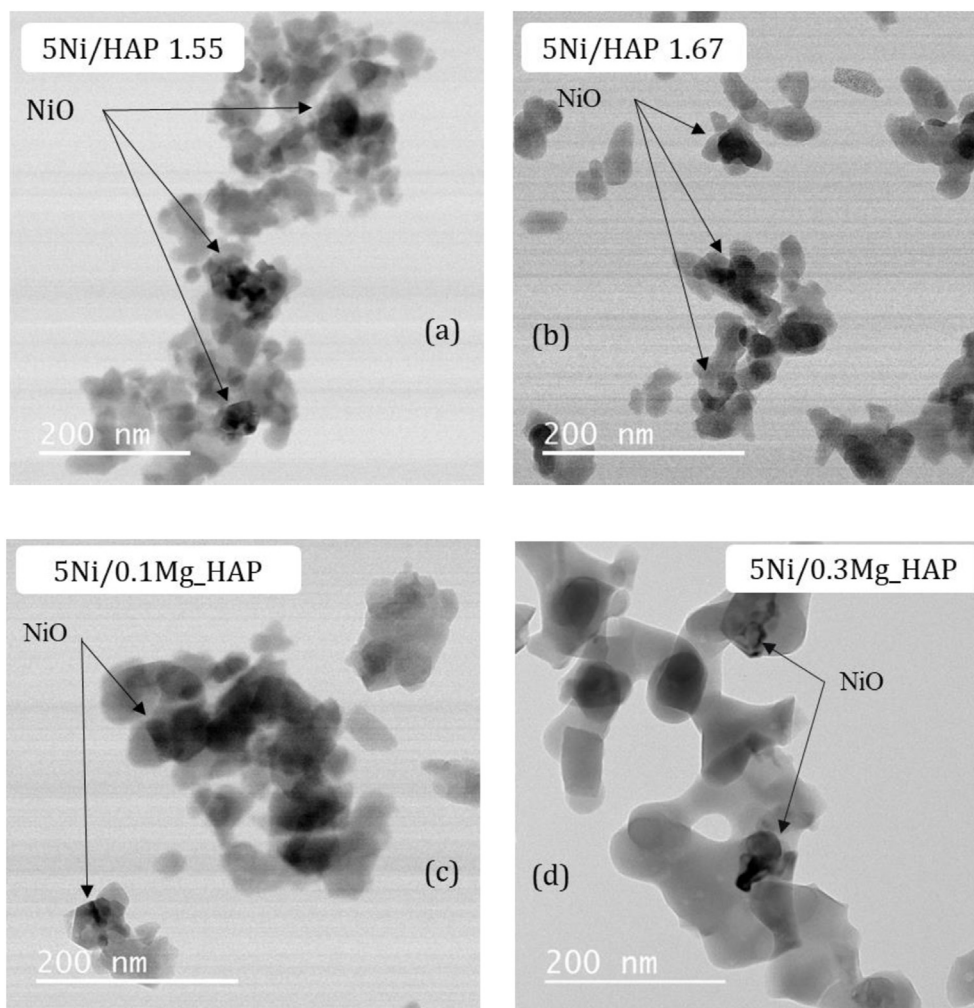


Fig. 5 – TEM images and particle size distribution of selected Ni/HAP and Ni/Mg_HAP catalysts.

curves, in comparison with those of the corresponding supports.

The treatment of these isotherms by the BET and BJH methods allowed obtaining the specific surface area (S_{BET}), the

porous volume (V_p) and the mean pore size (d_p) of each support and catalyst (Table 4). The HAP and Mg_HAP supports had relatively high S_{BET} (55–125 m^2/g). For HAP support, S_{BET} increased with the increase of the Ca/P ratio. For Mg_HAP

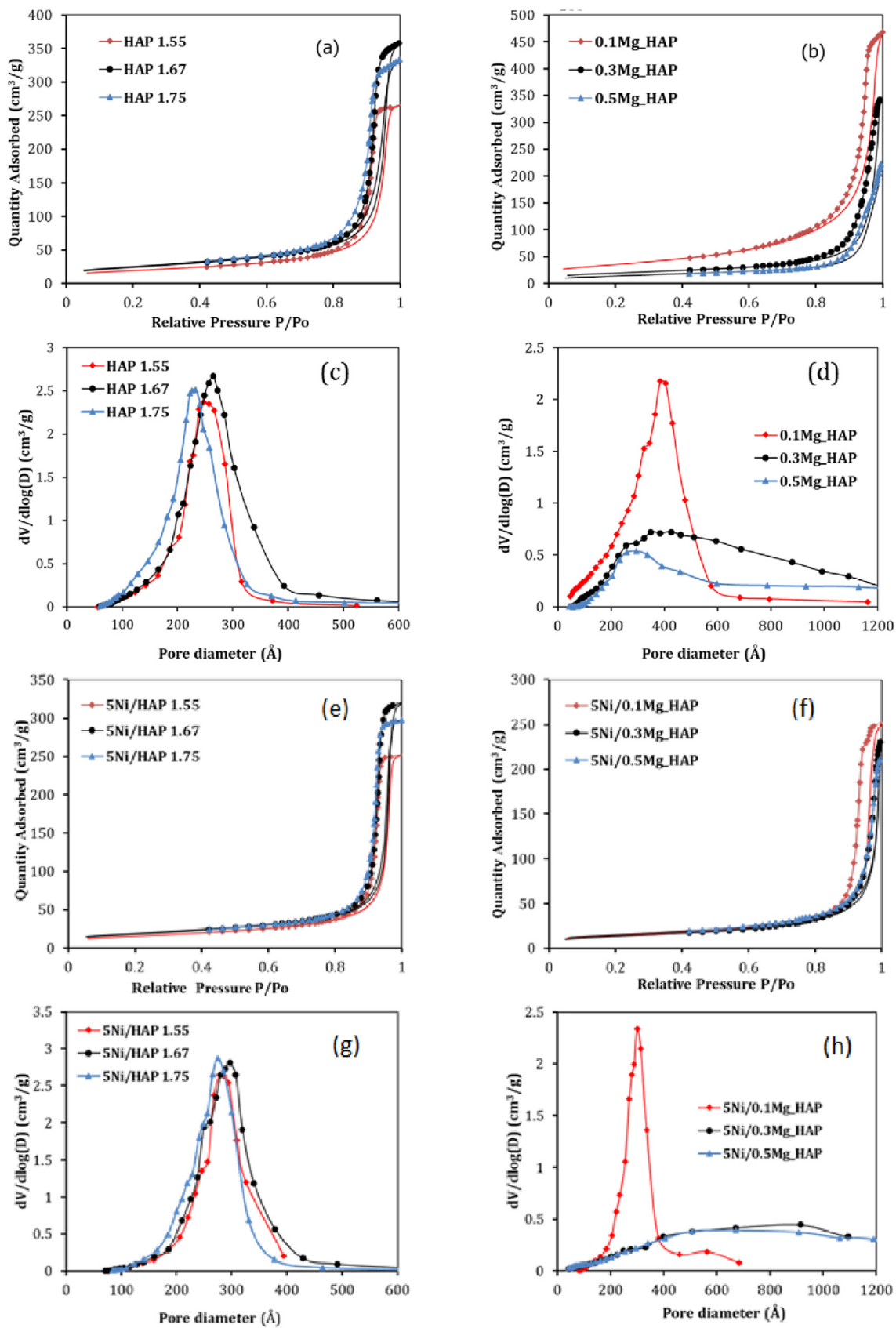


Fig. 6 – Nitrogen adsorption-desorption isotherms and differential pore size distribution of the supports and the catalysts.

Table 4 – Textural properties of the prepared supports and catalysts.

Material	S_{BET} (m^2/g)	V_p (cm^3/g)	d_p (nm)
HAP1.55	66	0.42	20.4
HAP1.67	86	0.57	22.4
HAP1.75	90	0.54	19.3
0.1 Mg_HAP	125	0.71	21.4
0.3 Mg_HAP	67	0.52	31.4
0.5 Mg_HAP	55	0.31	30.0
5Ni/HAP1.55	55	0.39	24.2
5Ni/HAP1.67	65	0.50	25.6
5Ni/HAP1.75	68	0.47	23.2
5Ni/0.1 Mg_HAP	50	0.39	26.3
5Ni/0.3 Mg_HAP	47	0.32	34.1
5Ni/0.5 Mg_HAP	52.1	0.30	30.2

supports, the incorporation of a small amount of Mg led to a strong increase of S_{BET} (125 m^2/g for 0.1 Mg_HAP containing 2.4 wt% Mg). Goldberg et al. [47] also found that the incorporation of 1 wt% of Mg into HAP structure led to a strong increase of S_{BET} . However, at higher Mg contents, S_{BET} strongly decreased (55–67 m^2/g for 0.3 Mg_HAP and 0.5 Mg_HAP supports). The deposition of Ni followed by the calcination at 700 °C led to a notable diminution of V_p and S_{BET} values, but to an increase of d_p . This suggests that nickel oxide nanoparticles were preferably formed inside the smallest pores, thus reducing V_p but increasing d_p . The reduction of V_p and S_{BET} could also be due to the effect of the calcination at 700 °C. In fact, Cacciotti et al. [53] showed that the calcination at 600 °C of a HAP substituted with 10 atomic % of Mg led to a reduction of S_{BET} from 87 to 27 $\text{m}^2 \text{g}^{-1}$.

TPR

Fig. 7 (a) shows TPR profiles of Ni/HAP and Ni/Mg_HAP catalysts, which were previously calcined at 700 °C. This calcination should convert nickel nitrate into nickel oxide (NiO) as evidenced by XRD analysis. It was already reported in the literature that the reduction of nickel oxide occurred through three consecutive steps: the first takes place within 300 and 400 °C (peak noted as α), which is due to the reduction of nickel species having weak interaction with the support; the second happens within 400 and 500 °C (peak noted as β), which corresponds to the reduction of nickel species having strong interaction with the support; and the third is found above 500 °C (peak noted as γ), which is related to the reduction of nickel species incorporated in the structure of the support [22, 23]. For Ni/HAP catalysts and 5Ni/0.1 Mg_HAP catalyst (Fig. 7 a), the TPR profiles were similar to each other: Each catalyst displayed three reduction peaks, which were more or less overlapped, with β peak as the principal one. In addition, it seemed that the intensity of γ peak was more important for 5Ni/HAP1.55 and 5Ni/0.1 Mg_HAP than for 5Ni/HAP1.67 and 5Ni/HAP1.75. In fact, during the catalyst synthesis by impregnation, cation exchange between Ni^{2+} and Ca^{2+} and/or Mg^{2+} could take place [34]. ICP-AES analysis showed that 5Ni/HAP1.67 and 5Ni/HAP1.75 catalysts had the similar Ca/P ratio of 1.73 and 1.74. These calcium-surplus materials are not favorable for the cation exchange, as previously observed by Boukha et al. [23]. Thus, the intensity of γ peak of these catalysts were weak. On the other hand, the 5Ni/HAP1.55 catalyst

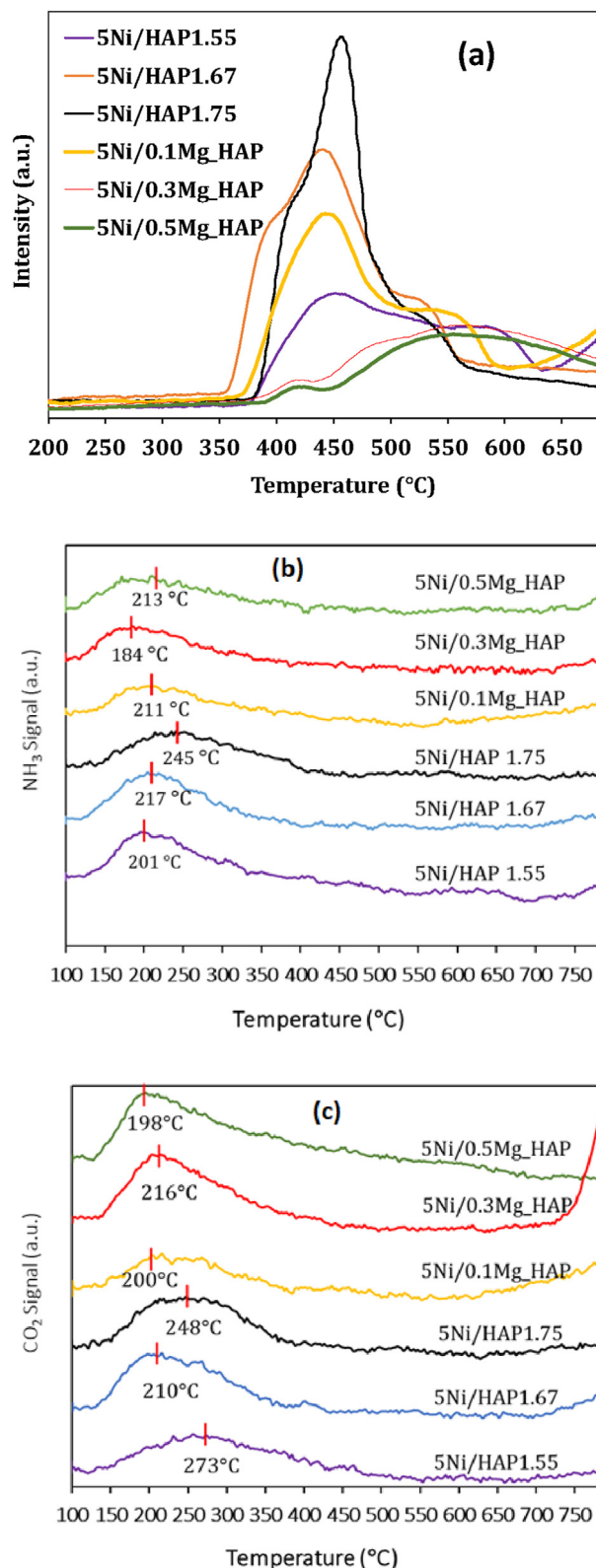


Fig. 7 – (a) TPR profiles; (b) NH_3 -TPD profiles; and (c) CO_2 -TPD profiles of the prepared catalysts.

was a calcium-deficient material (Ca/P ratio of 1.61 by ICP-AES), which must favor the cation exchange [23]. However, for 5Ni/0.1 Mg_HAP catalyst, despite its high (Ca + Mg)/P ratio of 1.82, the intensity of its γ peak was relatively important.

Was the solid solution of nickel and magnesium oxides formed? Further characterization such as XPS would be useful to better understand this behavior.

For 5Ni/0.3 Mg_HAP and 5Ni/0.5 Mg_HAP catalysts, their (Ca + Mg)/P ratio, which was determined by ICP-AES, reached 1.81 and 1.64, respectively. However, their TPR profiles are similar to each other with a small α peak at around 430 °C, and a large overlapped β and γ peak around 500–580 °C. In comparison to Ni/HAP catalysts, TPR peaks of 5Ni/0.3 Mg_HAP and 5Ni/0.5 Mg_HAP shifted to higher temperatures, meaning a stronger metal-support interaction, which is generally favorable for the thermal stability of the catalyst in DRM reaction [22,54].

Fig. 7 (b) presents NH₃-TPD profiles of the reduced catalysts (see experimental section for the TPD procedure). In all cases, a desorption peak was observed within 130 et 400 °C. This desorption temperature range suggests the presence of acidic sites of weak and moderate strength. Above 400 °C, TCD signals were not significant. However, above 750 °C, some TCD signals could be detected, which might be due to the emission of carbon dioxide from decarbonation of carbonate groups inserted in the apatitic structure [23].

Fig. 7 (c) shows CO₂-TPD profiles of the six catalysts. A broad desorption peak at around 130–500 °C was observed for all the catalysts, indicating the presence of basic sites of weak and moderate strength. TCD signals observed above 750 °C might be attributed to the decarbonation of carbonate groups, as observed for NH₃-TPD.

From TPD curves, the temperatures of TPD peaks and the density of acidic and basic sites could be determined (Table 5). Thus, all the six catalysts contained both acidic and basic sites. As expected, the increase of Ca/P ratio in HAP supports and the incorporation of Mg in Mg_HAP supports allowed decreasing the acidity and increasing the basicity of the catalysts.

Catalytic results

Impact of catalyst supports in DRM

Fig. 8 compared the activity and the selectivity of the six catalysts in DRM reaction under the same reaction conditions. Before starting the reaction, all the catalysts were in-situ reduced under H₂ at 700 °C. For HAP-supported nickel catalysts, 5Ni/HAP1.67 and 5Ni/HAP1.75 had the similar catalytic behavior, taking into account their similar composition and structure, as evidenced by different

characterizations (ICP-AES, XRD, TPR, TPD, etc.). The initial CH₄ and CO₂ conversion reached 73 and 77%, respectively, which decreased to 65 and 75% after the first 5 h of time-on-stream (TOS), indicating that a catalytic deactivation took place. The catalytic activity of these catalysts was relatively stable after ca. 45 h TOS at around 59 and 68% of CH₄ and CO₂ conversion, respectively. For 5Ni/HAP1.55 catalyst, it was less active than 5Ni/HAP1.67 and 5Ni/HAP1.75. The CH₄ and CO₂ conversion decreased from 45 to 58% at the beginning to 44 and 56% after 50 h TOS, respectively. This can be explained by the impact of Ca/P ratio of HAP support. 5Ni/HAP1.55 catalyst had the lowest Ca/P ratio, leading to a higher acidity and a lower basicity in comparison with 5Ni/HAP1.67 and 5Ni/HAP1.75 catalysts (Table 5). High basicity favors CO₂ adsorption, and so accelerates methane reforming in DRM [55,56]. However, 5Ni/HAP1.55 catalyst was relatively stable along the reaction time (CH₄ and CO₂ conversion practically unchanged). Did the calcium deficiency in HAP1.55 support better stabilize nickel nanoparticles in DRM at 700 °C? This might be possible since the surface of this support can better incorporate Ni²⁺ cations into its apatitic structure, as previously suggested by TPR results (Fig. 7 a).

For Mg_HAP-supported nickel catalysts, 5Ni/0.3 Mg_HAP and 5Ni/0.5 Mg_HAP showed similar catalytic behavior, which could be comparable to that of 5Ni/HAP1.67 and 5Ni/HAP1.75 catalysts. The initial CH₄ and CO₂ conversion reached nearly 73 and 77%, which became relatively stable above 45 h TOS at around 53 and 64%, respectively. On the other hand, 5Ni/ 0.1 Mg_HAP catalyst was less active than 5Ni/0.3 Mg_HAP and 5Ni/0.5 Mg_HAP catalysts, and this once again evidenced the favorable impact of the basicity of catalyst in DRM reaction (Table 5). However, a very good catalytic stability of 5Ni/ 0.1 Mg_HAP catalyst was obtained along the DRM reaction, as previously observed for 5Ni/HAP1.55 catalyst. The molar ratio of Ca/P of the support 0.1 Mg_HAP reached 1.60, which is smaller than the stoichiometric value (Table 2), and which can better stabilize Ni species or Ni nanoparticles on the surface of the support. In addition, the role of Mg on the catalyst stability should be further evidenced. Did the addition of small Mg amount in 5Ni/0.1 Mg_HAP catalyst improve the catalytic stability? Further study, in particular the characterization of the catalyst surface using techniques such as in-situ Diffuse Reflectance Infrared Fourier Transform Spectroscopy (DRIFTS), X-ray Photoelectron Spectroscopy (XPS), would be helpful to explain the catalytic behavior of this catalyst in DRM.

Table 5 – Acidic-basic properties of the prepared catalysts after in-situ reduction at 700 °C under H₂.

Catalyst	NH ₃ -TPD		CO ₂ -TPD	
	Peak temperature (°C)	Concentration of acidic sites (μmol/g)	Peak temperature (°C)	Concentration of basic sites (μmol/g)
5Ni/HAP1.55	201	121.9	273	121.4
5Ni/HAP1.67	217	94.9	210	167.4
5Ni/HAP1.75	245	86.9	248	168.6
5Ni/0.1 Mg_HAP	211	75.7	200	164.9
5Ni/0.3 Mg_HAP	184	75.6	216	185.6
5Ni/0.5 Mg_HAP	213	71.8	198	173.0

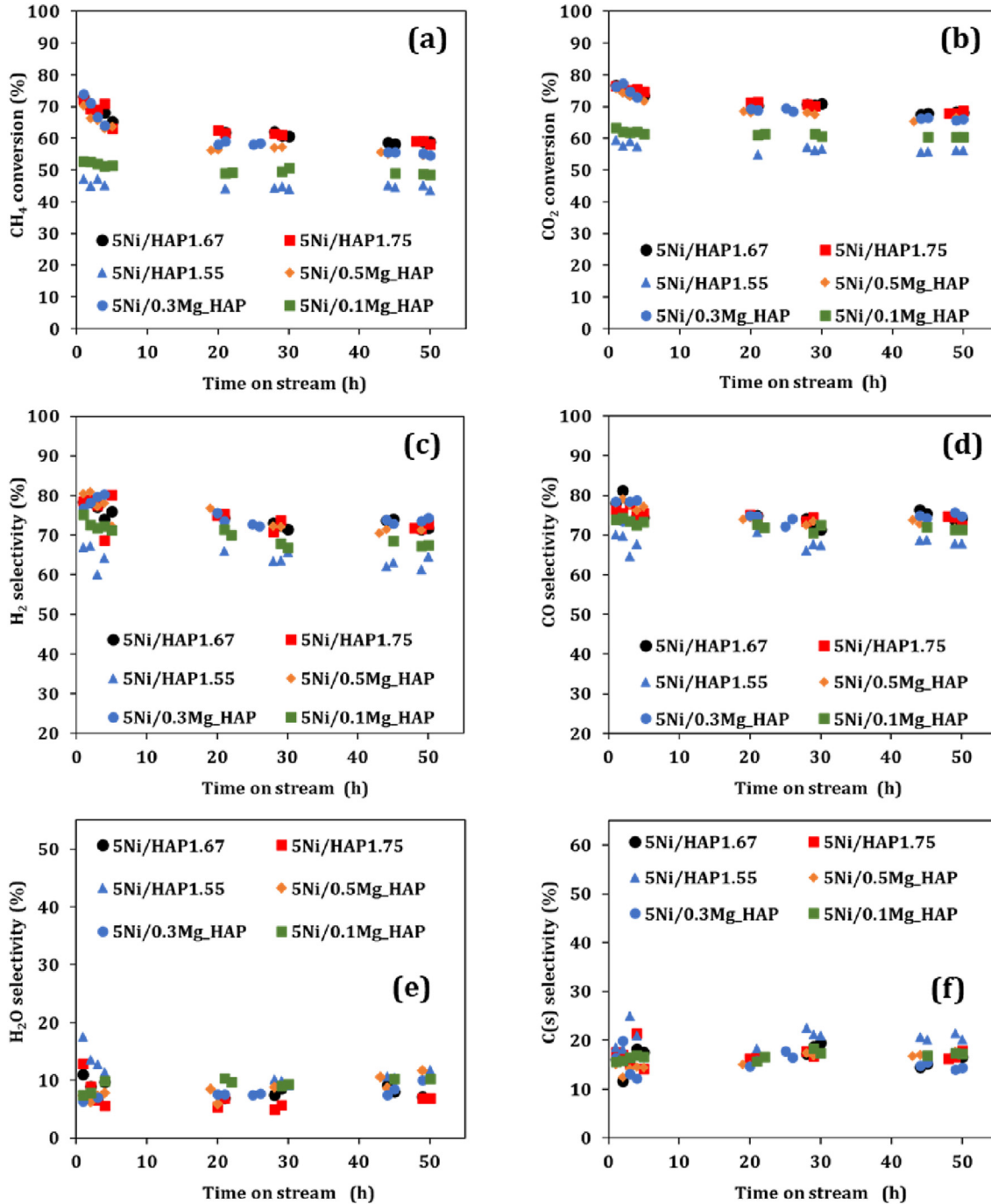
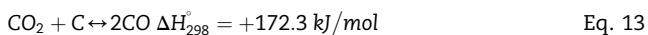
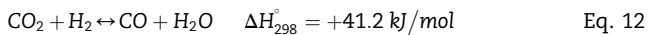


Fig. 8 – DRM reaction over HAP and Mg₂HAP supported nickel catalysts. Reaction conditions: feeding composition CH₄/CO₂/N₂ = 20%/20%/60% (vol%), GHSV = 31.7 L·h⁻¹·g_{cat}⁻¹, T = 700 °C, P = 1.8 bar.

It is worth noticing that, for each investigated catalyst, CO₂ conversion was systematically higher than CH₄ conversion. This indicating the presence of reactions favoring the consumption of CO₂, such as the *reversed water-gas shift* (Eq. (12)) and *reversed Boudouard reaction* (Eq. (13)), which was already observed in DRM by other groups [57].



By comparing the CH₄ and CO₂ conversion of the six prepared catalysts, the following decreasing order of catalytic activity can be classified: 5Ni/HAP1.75 ≈ 5Ni/HAP1.67 > 5Ni/0.3 Mg₂HAP ≈ 5Ni/0.5 Mg₂HAP > 5Ni/0.1 Mg₂HAP > 5Ni/HAP1.55. The addition of Mg did not allow improving the catalytic performance of Ni/HAP catalysts, but seemed to favor the catalytic stability.

H₂ and CO are the main targeted products of DRM reaction. Fig. 8 (c) and (d) shows that the four catalysts 5Ni/HAP1.67, 5Ni/HAP1.75, 5Ni/0.3 Mg₂HAP and 5Ni/0.5 Mg₂HAP, with the highest

catalytic activity, possessed also the highest selectivity in syn-gas. During the reaction, the selectivity into H_2 and CO slightly decreased from ca. $85 \pm 3\%$ at the beginning of the reaction to ca. $80 \pm 3\%$ at 50 h TOS. 5Ni/HAP1.55 and 5Ni/0.1 Mg_HAP catalysts, having the lowest catalyst activity, had also smaller selectivity in H_2 and CO, which was within the range of 80–75%.

Water and solid carbon are the two by-products of DRM. In Fig. 8 (e), the selectivity of water, quantified during the DRM reaction, was found within the range of 5–14%, which was relatively stable for each catalyst. About the solid carbon, as mentioned in the experimental section, its amount could not be experimentally measured during the reaction, but could be calculated from the carbon balance. Thus, the selectivity in solid carbon was found in the range of 6–13% for all the catalysts (Fig. 8 (f)).

The formation of solid carbon is one of the main reasons of catalyst deactivation. Thus, the used catalysts recovered after DRM reaction were characterized to better understand the nature of this solid carbon. Generally, solid carbon formed during a catalytic reaction can exist under various forms of graphitic carbon, fibrous carbon (whisker), or carbon nanotube (CNT) [58,59]. In Supplementary information SI 8, fibrous carbon was omnipresent on the surface of all the six used catalysts. On the other hand, graphitic carbon was particularly present in the case of 5Ni/HAP1.55, which explains the lowest catalytic activity of this catalyst.

Another reason of catalyst deactivation for high temperature processes such as in the case of DRM reaction is the thermal sintering of metal nanoparticles. Thus, TEM-EDX analysis was conducted with the following used catalysts: 5Ni/HAP1.55, 5Ni/HAP1.67, 5Ni/0.1 Mg_HAP et 5Ni/ 0.3 Mg_HAP. In fact, 5Ni/HAP1.67 and 5Ni/0.3 Mg_HAP were similar to 5Ni/HAP1.75 5Ni/0.5 Mg_HAP, respectively, so we did not analyze the used 5Ni/HAP1.75 and 5Ni/0.5 Mg_HAP catalysts. Fig. 9 shows some TEM images of these used catalysts. In addition to the relatively-large Ni nanoparticles, which were already observed with the fresh catalysts (Fig. 5), a population of small Ni nanoparticles of a dozen nm could be also observed. The presence of this population of small Ni nanoparticles was confirmed by EDX analysis (Supplementary information: SI 9 to SI 12). It might be possible that these small Ni nanoparticles were formed under the in-situ reduction (before the catalytic test) and/or during the DRM reaction from Ni^{2+} cations inserted into the apatitic structure of the support by cation exchange. This transformation could not take place during the calcination under the air at 700 °C. Thus, since TEM analysis was not conducted with fresh reduced catalysts, it is not possible to conclude on the catalyst sintering. But, from the catalytic results and from TEM images of the used catalysts, we can suppose that the thermal sintering must not be significant in the case of the catalysts investigated in this study.

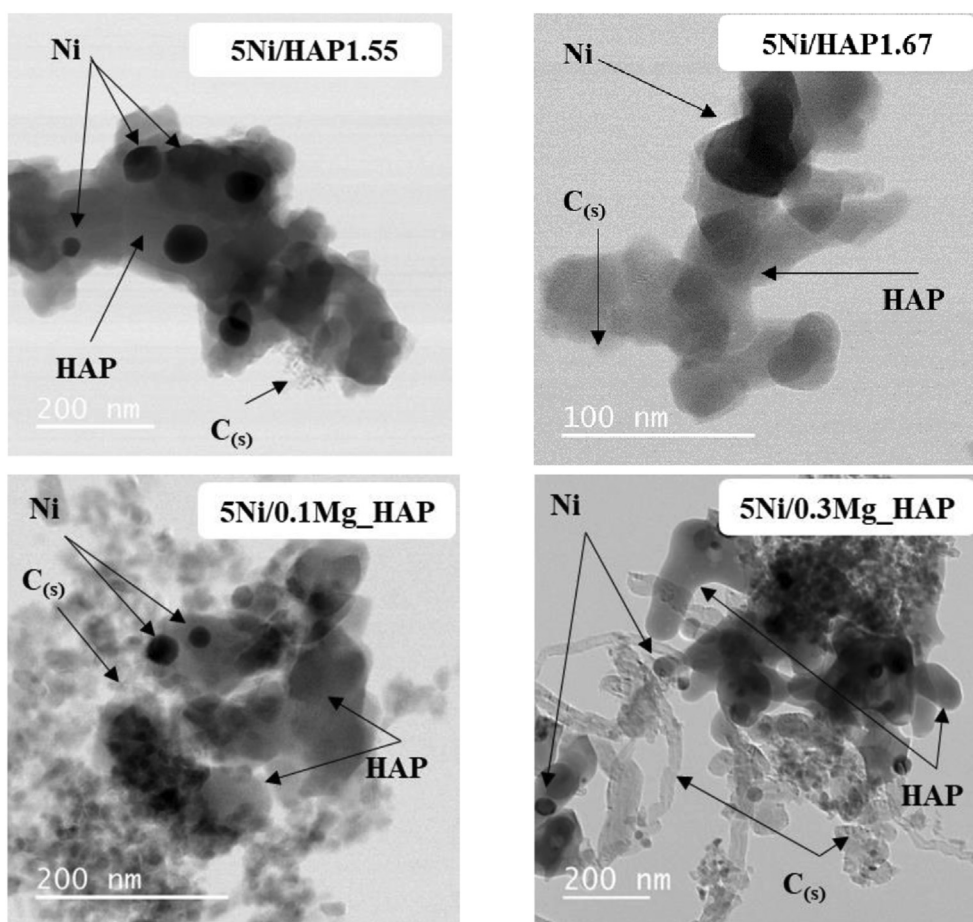


Fig. 9 – TEM images of the four used catalysts recovered after DRM reaction at 700 °C.

Table 6 – Pressure drop as a function of GHSV in DRM reaction over 5Ni/HAP1.67 catalyst.

Catalyst	GHSV ($L \cdot g_{cat}^{-1} \cdot h^{-1}$)	Pressure drop at the beginning of the reaction (bar)	Pressure drop at 50 h TOS (bar)
5Ni/HAP1.67	15.8	0.75	0.88
	31.7	1.60	1.80
	47.6	2.50	3.20

Impact of reaction conditions

Impact of the contact time. The impact of the contact time was studied over 5Ni/HAP1.67 and Ni/HAP1.55 catalysts, since 5Ni/HAP1.67 had the best catalytic performance while Ni/HAP1.55 had a very good catalyst stability among the six prepared catalysts, as previously shown in Fig. 8. For this study, the catalyst amount was kept unchanged (340 mg), while three total feeding flowrates were employed: 90, 180, and 270 NmL/min, which correspond to three GHSV of 15.8, 31.7 and 47.6 $L \cdot g_{cat}^{-1} \cdot h^{-1}$. The inlet gas was composed of 20%CH₄, 20%CO₂ and 60%N₂ (vol%), while the reaction temperature was fixed at 700 °C. Before the reaction, the catalyst was also *in-situ* reduced at 700 °C under a flux of 10 vol%H₂/N₂ for 2 h. On the other hand, a variation of the pressure drop inside the reactor

as a function of GHSV was observed, as shown in Table 6 in the case of 5Ni/HAP1.67, which was due to fine alumina powder used to charge the reactor. This pressure drop slightly increased during the reaction, which must be due to the accumulation of solid carbon inside the catalyst bed.

Fig. 10 shows the CH₄ and CO₂ conversion over 5Ni/HAP1.67 and Ni/HAP1.55 catalysts at different GHSV.

In the case of 5Ni/HAP1.67, for each GHSV employed, the catalytic behavior of this catalyst was similar, with a progressive catalyst deactivation up to around 45 h TOS, before reaching a relative stabilization. As expected, the increase of GHSV led to a decrease in CH₄ and CO₂ conversion. For example, CH₄ conversion diminished from 83 to 72%, 72 to 57%, and 61 to 44% after 45 h TOS, at GHSV of 15.8, 31.7 and 47.6 $L \cdot g_{cat}^{-1} \cdot h^{-1}$, respectively (Fig. 10 (a)). The increase of GHSV reduced the probability of reactants to be converted into products, explaining the diminution of the reaction conversion. In the case of the present study, the increase of pressure drop when the GHSV increased must also contribute to lower CH₄ and CO₂ conversions. For all GHSV investigated, CO and H₂ were the main products formed with selectivity within 85–95%, while water and solid carbon were the two byproducts of the reaction (results not shown).

In the case of Ni/HAP1.55 catalyst, as previously observed in Fig. 8, this catalyst showed a very good catalyst stability along

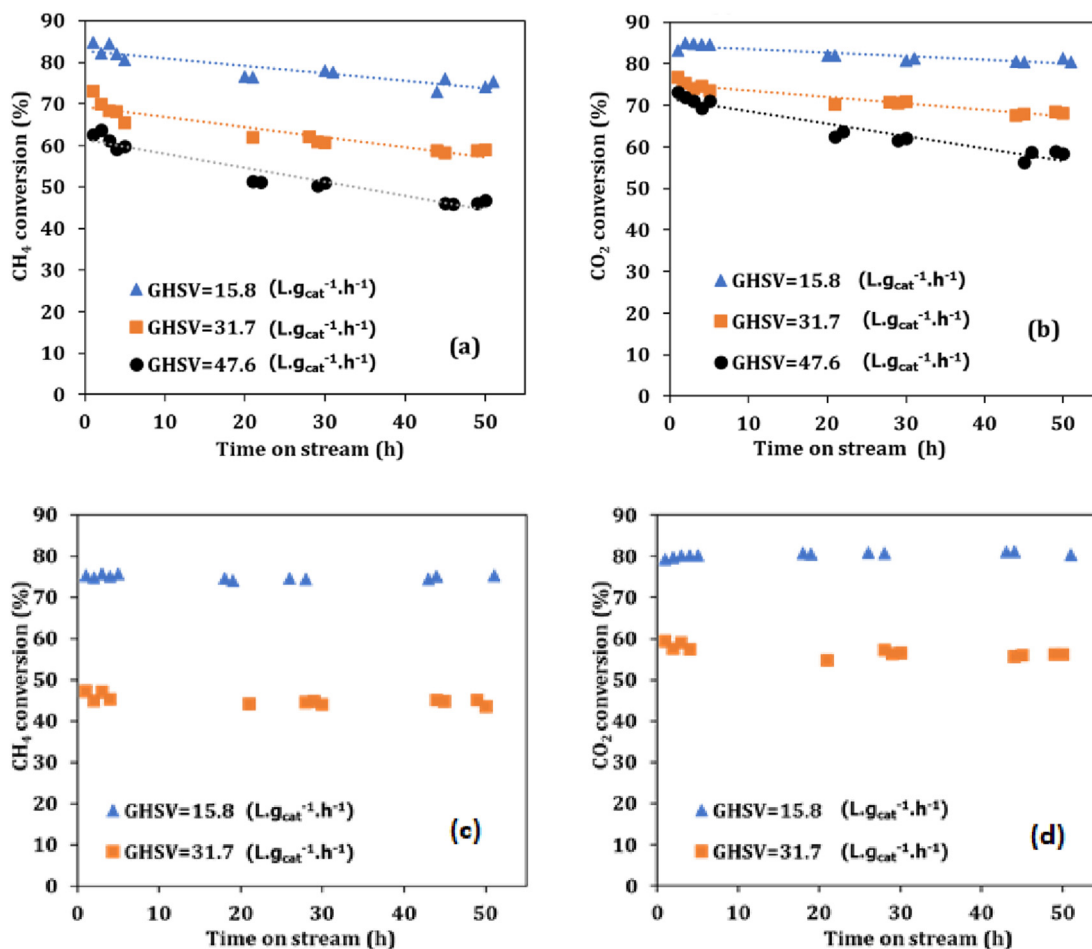


Fig. 10 – Impact of GHSV on the catalytic performance at 700 °C of: (a) and (b) 5Ni/HAP1.67; (c) and (d) Ni/HAP1.55 catalyst.

the DRM reaction. To verify this catalytic behavior, this catalyst was investigated at two GHSV of 15.8 and 31.7 $\text{L}\cdot\text{g}_{\text{cat}}^{-1}\cdot\text{h}^{-1}$. Fig. 10 (c) and (d) confirmed this catalytic stability along the reaction time at both GHSV investigated. The conversions of CH_4 and CO_2 were well stable along the reaction. Very high selectivity into H_2 and CO were also observed in all case, while water and solid carbon as two byproducts of the reaction were formed at low amounts (results not shown).

Impact of the reaction temperature and the total pressure. DRM reaction is highly endothermic (Eq. (1)), so it is strongly impacted by the reaction temperature. Fig. 11 (a) and (b) show the CH_4 and CO_2 conversions over 5Ni/HAP1.67 catalyst at 700 and 800 °C and GHSV of 47.6 $\text{L}\cdot\text{g}_{\text{cat}}^{-1}\cdot\text{h}^{-1}$. A mixture containing 50 vol% CH_4 and 50 vol% CO_2 (instead of 20% CH_4 , 20% CO_2 and 60% N_2 in previous sections) was used, in order to keep the reaction conversion under the thermodynamic limit at 700 and 800 °C. At 700 °C, the initial CH_4 and CO_2 conversions (at the beginning of the reaction) reached 35 and 42%, which only slightly decreased to 31 and 40% at 25 h TOS. At 800 °C, the CH_4 and CO_2 conversions at the beginning of the reaction reached 54 and 60%, and 52 and 58% at 20 h TOS, respectively, and then remained stable. This catalytic stability at 800 °C was significant in DRM, suggesting a good resistance of the catalyst

against a possible risk of thermal sintering at this high temperature.

DRM reaction is thermodynamically favored at low pressure (e.g. ambient pressure) [2, 3, 4]. However, downstream processes of the syngas production are generally operated at higher pressure, e.g. 20 bar for Fischer–Tropsch synthesis. Thus, it would be interesting to conduct the syngas production at high pressures, which have advantages to avoid the expensive steps of syngas compression [60,61]. For example, hydrogen production at the pilot scale by steam reforming of biogas was performed at 16 bar [62]. Thus, in the present study, the impact of the total reaction pressure was investigated in the range of 3–15 bar, using 5Ni/HAP1.67 catalyst. The reaction temperature was fixed at 700 °C, while the feeding composition was 50 vol% CH_4 and 50 vol% CO_2 , with a total gas flowrate of 270 NmL/min , corresponding to a GHSV of 47.6 $\text{L}\cdot\text{g}_{\text{cat}}^{-1}\cdot\text{h}^{-1}$. Before test, the catalyst was also in-situ reduced at 700 °C under 10 vol% H_2/N_2 for 2 h. Fig. 11 (c) and (d) shows the results obtained. As expected, the CH_4 and CO_2 conversions decreased when the total reaction pressure increased. At 3 bar total pressure, an initial catalyst deactivation took place during ca. 45 h TOS before being relatively stable (ca. 42 and 55% of CH_4 and CO_2 conversion, respectively). The increase of the total pressure

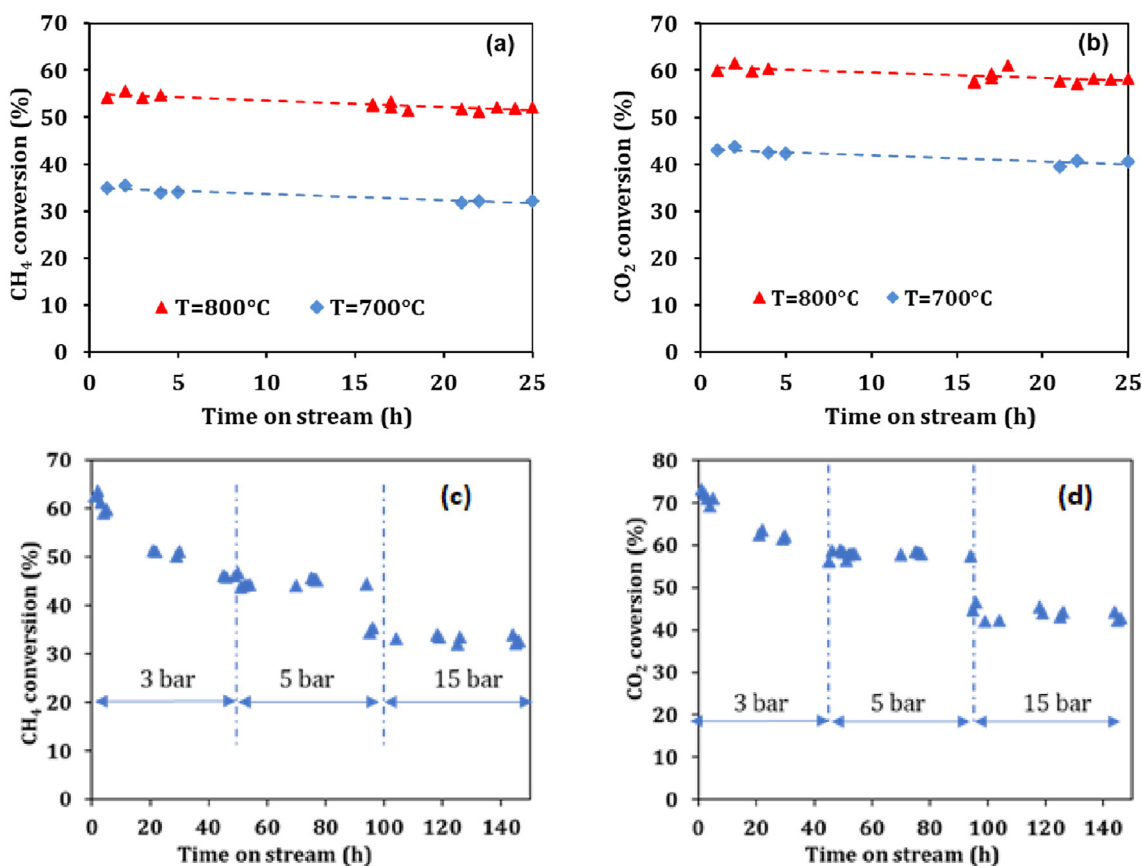


Fig. 11 – (a) and (b): Effect of the reaction temperature on the catalytic performance of 5Ni/HAP1.67 catalysts. Reaction conditions: total pressure = 1.7–1.9 bar; catalyst mass = 340 mg (In-situ reduction under 10 vol% H_2/N_2 for 2 h); GHSV = 47.6 $\text{L}\cdot\text{g}_{\text{cat}}^{-1}\cdot\text{h}^{-1}$; feeding composition: $\text{CH}_4/\text{CO}_2 = 50 \text{ vol}\%/50 \text{ vol}\%$. (c) and (d): Impact of the total pressure on the catalytic performance of 5Ni/HAP1.67 catalyst. Reaction conditions: Total pressure = 3, 5 and 15 bar; T = 700 °C; catalyst mass = 340 mg (In-situ reduction under 10 vol% H_2/N_2 for 2 h); GHSV = 47.6 $\text{L}\cdot\text{g}_{\text{cat}}^{-1}\cdot\text{h}^{-1}$, feeding composition: $\text{CH}_4/\text{CO}_2 = 50 \text{ vol}\%/50 \text{ vol}\%$.

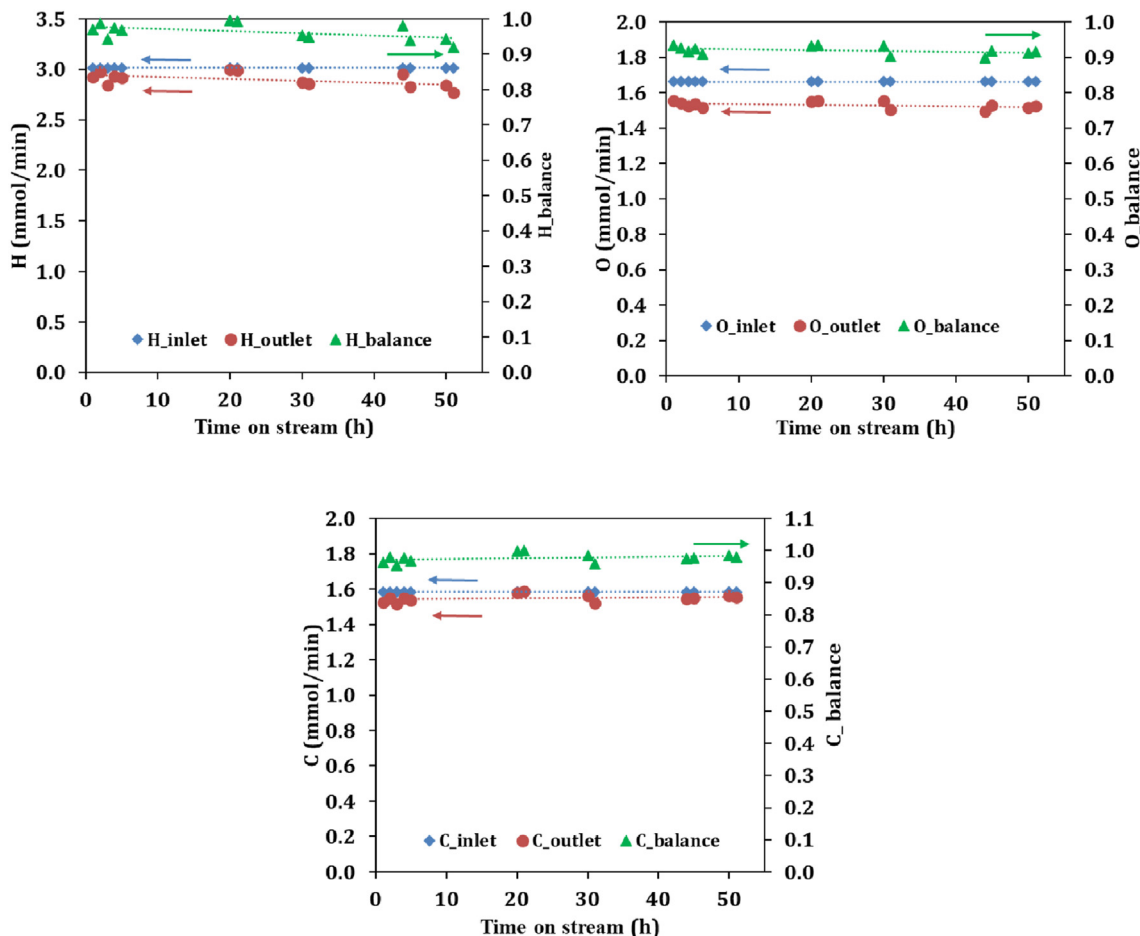


Fig. 12 – Mass balance in the DRM reaction over 5Ni/HAP1.67 at 700 °C and GHSV of 15.8 L·g_{cat}⁻¹·h⁻¹.

to 5 bar slightly decreased the CH₄ and CO₂ conversion to ca. 40 and 53%, respectively, without impacting the catalyst stability within 50–100 h TOS. Finally, when the total pressure increased to 15 bar, a net impact on the catalyst performance could be observed: the CH₄ and CO₂ conversion decreased to ca. 29 and 40%, respectively. Despite these low conversions, the catalyst remained relatively stable within 100–140 h TOS.

Mass balance

Mass balance was calculated for all three elements (C, O, and H) involved in the DRM reaction. The details of these calculations have been described elsewhere [26]. Briefly, from the total gas flowrate and the composition by μ -GC of the gas mixture at the reactor outlet (for permanent gases, e.g. CH₄, CO₂, CO, H₂) and water quantity (by water trap), it is possible to calculate the inlet flowrate and outlet flowrate of C, O, and H. The mass balance is then obtained by Eq. (14).

$$X_{\text{balance}} = \frac{X_{\text{outlet}}}{X_{\text{inlet}}} \quad \text{Eq. 14}$$

where X_{balance} : mass balance of C, O or H; X_{inlet} : inlet flowrate of X (mmol/min); X_{outlet} : outlet flowrate of X (mmol/min).

For all the catalytic tests conducted, the mass balance was relatively well buckled. As an example, Fig. 12 shows the case

of the test performed at 700 °C over 5Ni/HAP1.67 catalyst. The mass balance of all three elements reached above 90% meaning that most of the products of the reaction were well quantified.

Relative comparison

Table 7 presents a relative comparison of the catalytic performance of 5Ni/HAP1.67 catalyst developed in this study with those reported in the literature for DRM reaction. The terms $\text{TOF}_{\text{CH}_4}^{\text{mean}} (\text{mol}_{\text{CH}_4}^{\text{converted}} \cdot \text{mol}_{\text{Ni}_{\text{total}}}^{-1} \cdot \text{h}^{-1})$ and $\text{TOF}_{\text{CO}_2}^{\text{mean}} (\text{mol}_{\text{CO}_2}^{\text{converted}} \cdot \text{mol}_{\text{Ni}_{\text{total}}}^{-1} \cdot \text{h}^{-1})$ are calculated on the basis of the total quantity of Ni used in the catalytic test (but not the surface nickel amount, which were not systematically available). The values of $\text{TOF}_{\text{CH}_4}^{\text{mean}}$ and $\text{TOF}_{\text{CO}_2}^{\text{mean}}$ obtained with 5Ni/HAP1.67 catalyst were found to be only smaller than those of NiCe/SBA-16, Ni/MgO-Al₂O₃ and NiCeAl catalysts. Considering the fact that size distribution of nickel nanoparticles of 5Ni/HAP1.67 catalyst prepared in this work is found within a large range of 14–120 nm (Fig. 5), it would be helpful to reduce the size of these nickel nanoparticles in order to improve not only the activity, but also the stability of HAP-supported nickel catalysts. For that, other methods for nickel deposition on HAP supports would be investigated [33].

Table 7 – Relative comparison of the catalytic performance of 5Ni/HAP1.67 catalyst developed in the present study with those reported in the literature in DRM reaction; S: selectivity into a given product among H₂, CO, H₂O, C.

Catalyst	Ni loading (wt.%)	Reaction temperature (°C)	Total pressure (bar)	Q _{CH₄} ^{light} (mL/min)	Q _{CH₄} ^{total} (mL/min)	TOF _{CH₄} ^{mean} (mol _{CH₄} ^{converted} · mol _{Ni_{total}} ⁻¹ · h ⁻¹) during (x) h	TOF _{CO₂} ^{mean} (mol _{CO₂} ^{converted} · mol _{Ni_{total}} ⁻¹ · h ⁻¹) during (x) h	S _{H₂} , %	S _{CO} , %	S _{H₂O} , %	S _C , %	Ref.
5Ni/HAP1.67	3.96	800	1.7	54	54	350-250 (50)	413-323 (50)	80	82	7	10	This study
5Ni/HAP1.67	3.96	700	1.7	18	18	275-218 (50)	290-255 (50)	95	88	5	5	This study
Ni/Ca-HA	5.7	700	1.6	18	18	121 (7)	121 (7)	80	95	10	7	[24]
Ni/La ₂ O ₃	4.4	800	1	15	15	236 (12)	279 (12)	–	–	–	–	[63]
Ni-Mo ₂ C/La ₂ O ₃	4.4	800	1	15	15	138-138 (20)	197-197 (20)	–	–	–	–	[63]
NiCe/SBA-16	5	700	1	5	5	506-506 (100)	557-557 (100)	90	–	–	–	[64]
Ni/MgO-Al ₂ O ₃	10	750	1	49	49	552-552 (10)	638-638 (10)	–	–	–	–	[65]
Ni/MgO-Al ₂ O ₃	10	650	1	49	49	368-368 (10)	453-453 (10)	–	–	–	–	[65]
NiCeAl	7	700	1	30	30	477-465 (80)	–	–	84	–	–	[66]
Ni/CZ/SBA_15	10	600	1	10	10	21 (28)	36 (28)	–	–	–	–	[67]
Ni/CeO ₂	10	760	1	25	25	99-78 (105)	108-96(105)	–	–	–	–	[68]
Ni/CeO ₂ -3Ag	10	760	1	25	25	30-25 (105)	54-53(105)	–	–	–	–	[68]
2Ni1Co/ZSM5	7	700	1	20	20	268-192 (12)	293-252 (12)	63	64	–	–	[69]

Conclusions

This study aimed to investigate the synthesis, characterization and evaluation of calcium hydroxyapatite (HAP) and calcium hydroxyapatite-doped magnesium (Mg_HAP) supported nickel catalysts in dry reforming of methane (DRM) reaction. The synthesis of HAP supports containing various molar Ca/P ratios as well as Mg_HAP with various substitution levels of Ca²⁺ by Mg²⁺ in the apatitic structure could be achieved by simple wet precipitation method. Then, nickel nanoparticles with a large particle size distribution of 14–120 nm could be deposited on the support surface by incipient wetness impregnation. The prepared catalysts were mesoporous materials which had relatively high specific surface areas in the range of 47–68 m² g⁻¹ after air calcination at 700 °C. They contain both acidic and basic sites on the surface, which mostly had weak and moderate strength. The density of these sites depended on the composition of the supports. The catalyst prepared with calcium-deficient support (5Ni/HAP1.55) contained similar amounts of acidic and basic sites, while those prepared with calcium-surplus supports or Mg-doped supports had higher basic site density than acidic site density. TPR analysis indicated the presence of different nickel species, which had different strengths of interaction with the support. Among them, the strong metal-support interaction was found to be preponderant.

In DRM, the catalysts prepared with calcium-surplus supports (5Ni/HAP1.67 and 5Ni/HAP1.75) were more active than that prepared with calcium-deficient support (5Ni/HAP1.55). This could be explained by the impact of Ca/P ratio. High Ca/P ratio in calcium-surplus supports favored CO₂ adsorption and so favored the DRM reaction. However, the catalyst prepared with calcium-deficient support (5Ni/HAP1.55) was found to be more stable. The partial substitution of Ca²⁺ by Mg²⁺ in the apatitic structure did not improve the catalytic activity. On the other hand, the catalytic stability could be enhanced by small amount of Mg addition (in the case of 5Ni/0.1 Mg_HAP). This beneficial effect of Mg addition on the catalytic stability would be confirmed by further investigations. The impact of the reaction temperature and pressure could also be confirmed. According the thermodynamic properties of the DRM reaction, increasing the reaction temperature strongly favor the reaction conversion, while increasing the reaction pressure lowered the reaction conversion. In all cases, CO and H₂ were formed as the two main products, with the selectivity stabilized up to 85 ± 3%. At 700–800 °C, H₂O and solid carbon were still formed as undesirable products at notable amounts around 5–10% of selectivity.

Further work would be conducted on the catalyst preparation method to reduce the size of nickel nanoparticles, which must be helpful to improve the activity, selectivity, and the stability of HAP-based catalysts.

Declaration of competing interest

The authors declare that they have no known competing financial interests or personal relationships that could have appeared to influence the work reported in this paper.

Acknowledgement

This work is a part of the VABHYOGAZ3 project supported by the French “Programme d’Investissements d’Avenir” under supervision of ADEME, the French Energy and Environment Agency. The authors are grateful towards the ADEME for their support to this project. The authors also thank the technical assistance of the staff at the RAPSODEE center, UMR CNRS 5302, IMT Mines Albi.

- [1] Gary Grim R, To AT, Farberow CA, Hensley JE, Ruddy DA, Schaidle JA. Growing the bioeconomy through catalysis: a review of recent advancements in the production of fuels and chemicals from syngas-derived oxygenates. *ACS Catal* 2019;9:4145–72. <https://doi.org/10.1021/acscatal.8b03945>.
- [2] Pham Minh D, Phan TS, Grouset D, Nzihou A. Thermodynamic equilibrium study of methane reforming with carbon dioxide, water and oxygen. *J. Clean Ener. Technol.* 2018;6(4):309–13. <https://doi.org/10.18178/JOCT.2018.6.4.480>.
- [3] Nikoo MK, Amin NAS. Thermodynamic analysis of carbon dioxide reforming of methane in view of solid carbon formation. *Fuel Process Technol* 2011;92:678–91. <https://doi.org/10.1016/j.fuproc.2010.11.027>.
- [4] Chein RY, Chen YC, Yu CT, Chung JN. Thermodynamic analysis of dry reforming of CH_4 with CO_2 at high pressures. *J Nat Gas Sci Eng* 2015;28:617–29. <https://doi.org/10.1016/j.jngse.2015.07.001>.
- [5] Yentekakis IV, Panagiotopoulou P, Artemakis G. A review of recent efforts to promote dry reforming of methane (DRM) to syngas production via bimetallic catalyst formulations. *Appl Catal B Environ* 2021;296:120210. <https://doi.org/10.1016/j.apcatb.2021.120210>.
- [6] Wu L, Xie X, Ren H, Gao X. A short review on nickel-based catalysts in dry reforming of methane: influences of oxygen defects on anti-coking property. *Mater Today Proc* 2021;42:153–60. <https://doi.org/10.1016/j.matpr.2020.10.697>.
- [7] Nair MM, Kaliaguine S. Structured catalysts for dry reforming of methane. *New J Chem* 2016;40(5):4049–60. <https://doi.org/10.1039/C5NJ03268G>.
- [8] Labrecque R, Lavoie JM. Dry reforming of methane with CO_2 on an electron-activated iron catalytic bed. *Bioresour Technol* 2011;102:11244–8. <https://doi.org/10.1016/j.biortech.2011.09.088>.
- [9] A. N. T. Cao, C. Q. Pham, L. K. H. Pham, D. L. T. Nguyen, T. T. P. Pham, T. T. V. Tran, V. P. Nguyen, T. B. Nguyen, Q. V. Le, N. A. Nguyen, T. M. Nguyen, Boosted methane dry reforming for hydrogen generation on cobalt catalyst with small cerium dosage, *Int J Hydrogen Energy* <https://doi.org/10.1016/j.ijhydene.2021.11.077>.
- [10] Mizera A, Błaszczak P, Bochentyn B, Lach R, Drożdż E. Cu supported on various oxides as a candidate catalyst for dry methane reforming in DIR-SOFCs systems. *Int J Hydrogen Energy* 2022;47:25647–61. <https://doi.org/10.1016/j.ijhydene.2022.06.016>.
- [11] Ballarini A, Basile F, Benito P, Bersani I, Fornasari G, De Miguel S, Maina SCP, Vilella J, Vaccari A, Scelza Oa. Platinum supported on alkaline and alkaline earth metal-doped alumina as catalysts for dry reforming and partial oxidation of methane. *Appl Catal Gen* 2012;433–434:1–11. <https://doi.org/10.1016/j.apcata.2012.04.037>.
- [12] Rostrup-Nielsen JR, Hansen J-HB. CO_2 reforming of methane over transition metals. *J Catal* 1993;144:38–49. <https://doi.org/10.1006/jcat.1993.1312>.
- [13] Tran TQ, Pham Minh D, Phan TS, Pham QN, Nguyen Xuan H. Dry reforming of methane over calcium-deficient hydroxyapatite supported cobalt and nickel catalysts. *Chem Eng Sci* 2020;228:115975. <https://doi.org/10.1016/j.ces.2020.115975>.
- [14] Theofanidis SA, Batchu R, Galvita VV, Poelman H, Marin GB. Carbon gasification from Fe–Ni catalysts after methane dry reforming. *Appl Catal B Environ* 2016;185:42–55. <https://doi.org/10.1016/j.apcatb.2015.12.006>.
- [15] Boualouache A, Boucenna A. Mechanistic details of methane dry reforming on copper-nickel bimetallic surfaces. *Chem Phys Lett* 2020;739:136995. <https://doi.org/10.1016/j.cplett.2019.136995>.
- [16] Margossian T, Larmier K, Kim SM, Krumeich F, Müller C, Copéret C. Supported bimetallic NiFe nanoparticles through colloid synthesis for improved dry reforming performance. *ACS Catal* 2017;7:6942–8. <https://doi.org/10.1021/acscatal.7b02091>.
- [17] Teh LP, Setiabudi HD, Timmiati SN, Aziz MAA, Annuar NHR, Ruslan NN. Recent progress in ceria-based catalysts for the dry reforming of methane: a review. *Chem Eng Sci* 2021;239:116606. <https://doi.org/10.1016/j.ces.2021.116606>.
- [18] Ekeoma BC, Yusuf M, Johari K, Abdullah B. Mesoporous silica supported Ni-based catalysts for methane dry reforming: a review of recent studies. *Int J Hydrogen Energy* 2022;47(98):41596–620. <https://doi.org/10.1016/j.ijhydene.2022.05.297>.
- [19] Alipour Z, Borugadda VB, Wang H, Dalai AK. Chapter 8 - dry reforming of methane and biogas to produce syngas: a review of catalysts and process conditions. In: Nanda Sonil, Vo Dai-Viet N, Nguyen Van-Huy, editors. *Carbon dioxide capture and conversion*; 2022. p. 201–35. <https://doi.org/10.1016/B978-0-323-85585-3.00003-1>.
- [20] Hambali HU, Jalil AA, Abdulrasheed AA, Siang TJ, Gambo Y, Umar AA. Zeolite and clay based catalysts for CO_2 reforming of methane to syngas: a review. *Int J Hydrogen Energy* 2022;47:30759–87. <https://doi.org/10.1016/j.ijhydene.2021.12.214>.
- [21] Pham Minh D. Chapter 1- introduction to hydroxyapatite-based materials in heterogeneous catalysis. In: Pham Minh D, editor. *Design and applications of hydroxyapatite-based catalysts*. 1st ed. Wiley; 2022. p. 19–72. <https://doi.org/10.1002/9783527830190.ch1>.
- [22] Boukha Z, Kacimi M, Pereira MFR, Faria JL, Figueiredo JL, Ziyad M. Methane dry reforming on Ni loaded hydroxyapatite and fluoroapatite. *Appl Catal, A* 2007;317:299–309. <https://doi.org/10.1016/j.apcata.2006.10.029>.
- [23] Boukha Z, Yeste MP, Cauqui MÁ, González-Velasco JR. Influence of Ca/P ratio on the catalytic performance of Ni/hydroxyapatite samples in dry reforming of methane. *Appl Catal, A* 2019;580:34–45. <https://doi.org/10.1016/j.apcata.2019.04.034>.
- [24] Rego de Vasconcelos B, Pham Minh D, Martins E, Germeau A, Sharrock P, Nzihou A. Highly-efficient hydroxyapatite-supported nickel catalysts for dry reforming of methane. *Int J Hydrogen Energy* 2020;45(36):18502–18. <https://doi.org/10.1016/j.ijhydene.2019.08.068>.

- [25] Rego de Vasconcelos B, Pham Minh D, Sharrock P, Nzihou A. Regeneration study of Ni/hydroxyapatite spent catalyst from dry reforming. *Catal Today* 2018;310:107–15. <https://doi.org/10.1016/j.cattod.2017.05.092>.
- [26] Rêgo De Vasconcelos B, Zhao L, Sharrock P, Nzihou A, Pham Minh D. Catalytic transformation of carbon dioxide and methane into syngas over ruthenium and platinum supported hydroxyapatites. *Appl Surf Sci* 2016;390:141–56. <https://doi.org/10.1016/j.apsusc.2016.08.077>.
- [27] Wang YB, He L, Zhou BC, Sheng J, Fan J, Li WC. Anti-coking NiCe_x/HAP catalyst with well-balanced carbon formation and gasification in methane dry reforming. *Fuel* 2022;329:125477. <https://doi.org/10.1016/j.fuel.2022.125477>.
- [28] Meng J, Gu T, Pan W, Bu C, Zhang J, Wang X, Liu C, Xie H, Piao G. Promotional effects of defects on Ni/HAP catalyst for carbon resistance and durability during dry reforming of methane. *Fuel* 2022;310:122363. <https://doi.org/10.1016/j.fuel.2021.122363>.
- [29] Wang YB, He L, Zhou BC, Tang F, Fan J, Wang DQ, Lu AH, C Li W. Hydroxyapatite nanorods rich in [ca–o–p] sites stabilized ni species for methane dry reforming. *Ind Eng Chem Res* 2021;60:15064–73. <https://doi.org/10.1021/acs.iecr.1c02895>.
- [30] Li B, Yuan X, Li B, Wang X. Impact of pore structure on hydroxyapatite supported nickel catalysts (Ni/HAP) for dry reforming of methane. *Fuel Process Technol* 2020;202:106359. <https://doi.org/10.1016/j.fuproc.2020.106359>.
- [31] Verwilghen C, Rio S, Nzihou A, Gauthier D, Flamant G, Sharrock PJ. Preparation of high specific surface area hydroxyapatite for environmental applications. *J Mater Sci* 2007;42(15):6062–6. <https://doi.org/10.1007/s10853-006-1160-y>.
- [32] Basak M, Rahman ML, Ahmed MF, Biswas B, Sharmin N. The use of X-ray diffraction peak profile analysis to determine the structural parameters of cobalt ferrite nanoparticles using Debye-Scherrer, Williamson-Hall, Halder-Wagner and Size-strain plot: different precipitating agent approach. *J Alloys Compd* 2022;895:162694. <https://doi.org/10.1016/j.jallcom.2021.162694>.
- [33] El Jemli Y, Abdelouahdi K, Pham Minh D, Barakat A, Solhi A. Chapter 2: synthesis and characterization of hydroxyapatite and hydroxyapatite-based catalysts. In: Pham Minh D, editor. *Design and applications of hydroxyapatite-based catalysts*. 1st ed. Wiley; 2022. p. 19–72. <https://doi.org/10.1002/9783527830190.ch2>.
- [34] Pham Minh D, Rio S, Sharrock P, Sebei H, Lyczko N, Tran ND, Raii M, Nzihou A. Hydroxyapatite starting from calcium carbonate and orthophosphoric acid: synthesis, characterization, and applications. *J Mater Sci* 2014;49(12):4261–9. <https://doi.org/10.1007/s10853-014-8121-7>.
- [35] Diallo-Garcia S. Hydroxyapatites, un système basique atypique modulable par la synthèse : vers l'identification des sites actifs, PhD thesis. Université Pierre & Marie Curie; 2012. <https://www.theses.fr/2012PA066384>.
- [36] Ertl G, Knozinger H, Weitkamp J. *Handbook of heterogeneous catalysis*. Wiley; 1997.
- [37] Berzina-Cimdina L, Borodajenko N. Research of calcium phosphates using fourier transform infrared spectroscopy. In: Theophanides T, editor. *Infrared spectroscopy - materials science, engineering and technology*. InTech; 2012. <https://doi.org/10.5772/36942>.
- [38] Raynaud S, Champion E, Bernache-Assollant D, Thomas P. Calcium phosphate apatites with variable Ca/P atomic ratio I. Synthesis, characterisation and thermal stability of powders. *Biomaterials* 2002;23(4):1065–72. [https://doi.org/10.1016/S0142-9612\(01\)00218-6](https://doi.org/10.1016/S0142-9612(01)00218-6).
- [39] Cazalbou S, Combes C, Eichert D, Rey C. Adaptive physico-chemistry of bio-related calcium phosphates. *J Mater Chem* 2004;14(14):2148–53. <https://doi.org/10.1039/B401318B>.
- [40] Holcomb DW, Young RA. Thermal decomposition of human tooth enamel. *Calcif Tissue Int* 1980;31:189–201. <https://doi.org/10.1007/BF02407181>.
- [41] Meejoo S, Maneeprakorn W, Winotai P. Phase and thermal stability of nanocrystalline hydroxyapatite prepared via microwave heating. *Thermochim Acta* 2006;447(1):115–20. <https://doi.org/10.1016/j.tca.2006.04.013>.
- [42] Sader MS, Lewis K, Soares GA, LeGeros RZ. Simultaneous incorporation of magnesium and carbonate in apatite: effect on physico-chemical properties. *Mater Res* 2013;16(4):779–84. <https://doi.org/10.1590/S1516-14392013005000046>.
- [43] Pham Minh D, Lyczko N, Sebei H, Nzihou A, Sharrock P. Synthesis of calcium hydroxyapatite from calcium carbonate and different orthophosphate sources: a comparative study. *Mater Sci Eng, B* 2012;177(13):1080–9. <https://doi.org/10.1016/j.mseb.2012.05.007>.
- [44] Pham Minh D, Tran ND, Nzihou A, Sharrock P. Hydroxyapatite gel for the improved removal of Pb²⁺ ions from aqueous solution. *Chem Eng J* 2013;232:128–38. <https://doi.org/10.1016/j.cej.2013.07.086>.
- [45] Bigi A, Falini G, Foresti E, Gazzano M, Ripmonti A, Roveri N. Rietveld structure refinements of calcium hydroxylapatite containing magnesium. *Acta Crystallogr B* 1996;52(1):87–92. <https://doi.org/10.1107/S0108768195008615>.
- [46] Baravelli S, Bigi A, Ripamonti A, Roveri N, Foresti E. Thermal behavior of bone and synthetic hydroxyapatites submitted to magnesium interaction in aqueous medium. *J Inorg Biochem* 1984;20(1):1–12. [https://doi.org/10.1016/0162-0134\(84\)80001-X](https://doi.org/10.1016/0162-0134(84)80001-X).
- [47] Goldberg MA, Fomin AS, Murzakhanov FF, Makshakova ON, Donskaya NO, Antonova OS, Gnezdilov OI, Mikheev IV, Knotko AV, Kudryavtsev EA, Akhmedova SA, Sviridova IK, Sergeeva NS, Mamin GV, Barinov SM, Gafurov MR, Komlev VS. The improved textural properties, thermal stability, and cytocompatibility of mesoporous hydroxyapatite by Mg²⁺ doping. *Mater Chem Phys* 2022;289:126461. <https://doi.org/10.1016/j.matchemphys.2022.126461>.
- [48] Elliott JC. *Structure and chemistry of the apatites and other calcium orthophosphates*. Amsterdam: Elsevier; 1994.
- [49] Costentin G, Drouet C, Salles F, Sarda S. Chapter 3: structure and surface study of hydroxyapatite-based materials. In: Pham Minh D, editor. *Design and applications of hydroxyapatite-based catalysts*. 1st ed. Wiley; 2022. p. 73–140. <https://doi.org/10.1002/9783527830190.ch3>.
- [50] Fadeev IV, Shvorneva LI, Barinov SM, Orlovskii et VP. Synthesis and structure of magnesium-substituted hydroxyapatite. *Inorg Mater* 2003;39:947–50. <https://doi.org/10.1023/A:1025509305805>.
- [51] Sing KSW, Everett DH, Haul RAW, Moscou L, Pierotti RA, Rouqu erol J, Siemieniewska T. Reporting physisorption data for gas/solid systems with special reference to the determination of surface area and porosity. *Pure Appl Chem* 1985;57:603–19. <https://doi.org/10.1351/pac198557040603>.
- [52] Thomas M, Kaneko K, Neimark AV, Olivier JP, Rodriguez-Reinoso F, Rouqu erol J, Sing KSW. Physisorption of gases, with special reference to the evaluation of surface area and pore size distribution (UPAC Technical Report). *Pure Appl Chem* 2015;87:1051–69. <https://doi.org/10.1515/pac-2014-1117>.
- [53] Cacciotti I, Bianco A, Lombardi M, Montanaro L. Mg-substituted hydroxyapatite nanopowders: synthesis, thermal stability and sintering behaviour. *J Eur Ceram Soc*

- 2009;29:2969–78. <https://doi.org/10.1016/j.jeurceramsoc.2009.04.038>.
- [54] Goula MA, Charisiou ND, Papageridis KN, Delimitis A, Pachatouridou E, Iliopoulou EF. Nickel on alumina catalysts for the production of hydrogen rich mixtures via the biogas dry reforming reaction: influence of the synthesis method. *Int J Hydrogen Energy* 2015;40(30):9183–200. <https://doi.org/10.1016/j.ijhydene.2015.05.129>.
- [55] Titus J, Goepel M, Schunk SA, Wilde N, Gläser R. The role of acid/base properties in Ni/MgO-ZrO₂-based catalysts for dry reforming of methane. *Catal Commun* 2017;100:76–80. <https://doi.org/10.1016/j.catcom.2017.06.027>.
- [56] Gucci L, Stefler G, Geszti O, Sajo I, Paszti Z, Tompos A, Schay Z. Methane dry reforming with CO₂: a study on surface carbon species. *Appl Catal Gen* 2010;375(2):236–46. <https://doi.org/10.1016/j.apcata.2009.12.040>.
- [57] Arbag H, Yasyerli S, Yasyerli N, Dogu G. Activity and stability enhancement of Ni-MCM-41 catalysts by Rh incorporation for hydrogen from dry reforming of methane. *Int J Hydrogen Energy* 2010;35(6):2296–304. <https://doi.org/10.1016/j.ijhydene.2009.12.109>.
- [58] Rostrup-Nielsen JR. Catalytic steam reforming. In: Anderson JR, Boudart M, editors. *Catalysis. Catalysis*, 5. Berlin, Heidelberg: Springer; 1984. https://doi.org/10.1007/978-3-642-93247-2_1.
- [59] Helveg S, Sehested J, Rostrup-Nielsen JR. Whisker carbon in perspective. *Catal Today* 2011;178(1):42–6. <https://doi.org/10.1016/j.cattod.2011.06.023>.
- [60] Schulz LA, Kahle LCS, Delgado KH, Schunk SA, Jentys A, Deutschmann O, Lercher JA. On the coke deposition in dry reforming of methane at elevated pressures. *Appl Catal Gen* 2015;504:599–607. <https://doi.org/10.1016/j.apcata.2015.03.002>.
- [61] Mette K, Kühl S, Tarasov A, Willinger MG, Kröhnert J, Wrabetz S, Trunschke A, Scherzer M, Girgsdies F, Düdler H, Kähler K, Ortega KF, Muhler M, Schlögl R, Behrens M, Lunkenbein T. High-temperature stable Ni nanoparticles for the dry reforming of methane. *ACS Catal* 2016;6(10):7238–48. <https://doi.org/10.1021/acscatal.6b01683>.
- [62] T. S. Phan, D. Pham Minh, F. Espitalier, A. Nzihou, D. Grouset, Hydrogen production from biogas: Process optimization using ASPEN Plus®, *Int J Hydrogen Energy* <https://doi.org/10.1016/j.ijhydene.2022.01.100>.
- [63] Zhang M, Shi C, Chen B, Zhang Y, Zhu Y, Qiu J, Au C. Catalytic role of β-Mo₂C in DRM catalysts that contain Ni and Mo, *Catal. Today Off* 2015;258:676–83. <https://doi.org/10.1016/j.cattod.2015.01.014>.
- [64] Zhang S, Muratsugu S, Ishiguro N, Tada M. Ceria-doped Ni/SBA-16 catalysts for dry reforming of methane. *ACS Catal* 2013;3(8):1855–64. <https://doi.org/10.1021/cs400159w>.
- [65] Zhang L, Zhang Q, Liu Y, Zhang Y. Dry reforming of methane over Ni/MgO-Al₂O₃ catalysts prepared by two-step hydrothermal method. *Appl Surf Sci* 2016;389:25–33. <https://doi.org/10.1016/j.apsusc.2016.07.063>.
- [66] Wang N, Xu Z, Deng J, Shen K, Yu X, Qian W, Chu W, Wei F. One-pot synthesis of ordered mesoporous NiCeAl oxide catalysts and a study of their performance in methane dry reforming. *ChemCatChem* 2014;6(5):1470–80. <https://doi.org/10.1002/cctc.201300720>.
- [67] Albarazi A, Beaunier P, Da Costa P. Hydrogen and syngas production by methane dry reforming on SBA-15 supported nickel catalysts: on the effect of promotion by Ce_{0.75}Zr_{0.25}O₂ mixed oxide. *Int J Hydrogen Energy* 2013;38(1):127–39. <https://doi.org/10.1016/j.ijhydene.2012.10.063>.
- [68] Yu M, Zhu Y-A, Lu Y, Tong G, Zhu K, Zhou X. The promoting role of Ag in Ni-CeO₂ catalyzed CH₄-CO₂ dry reforming reaction. *Appl Catal B Environ* 2015;165:43–56. <https://doi.org/10.1016/j.apcatb.2014.09.066>.
- [69] Estephane J, Aouad S, Hany S, El Khoury B, Gennequin C, El Zakhem H, El Nakat J, Aboukais A, Abi Aad E. CO₂ reforming of methane over Ni-Co/ZSM5 catalysts. Aging and carbon deposition study. *Int J Hydrogen Energy* 2015;40(30):9201–8. <https://doi.org/10.1016/j.ijhydene.2015.05.147>.